SDSS-IV MaNGA: spatially resolved dust attenuation in spiral galaxies

Michael J. Greener,[1★] Alfonso Aragón-Salamanca,[1] Michael R. Merrifield,[1] Thomas G. Peterken,[1] Amelia Fraser-McKelvie,[1] Karen L. Masters,[2] Coleman M. Krawczyk,[3] Nicholas F. Boardman,[4] Médéric Boquien,[5] Brett H. Andrews,[6] Jonathan Brinkmann,[7] and Niv Drory[8]

[1] *School of Physics & Astronomy, University of Nottingham, University Park, Nottingham, NG7 2RD, UK*
[2] *Haverford College, Department of Physics and Astronomy, 370 Lancaster Avenue, Haverford, Pennsylvania 19041, USA*
[3] *Institute of Cosmology & Gravitation, University of Portsmouth, Dennis Sciama Building, Portsmouth, PO1 3FX, UK*
[4] *Department of Physics & Astronomy, University of Utah, Salt Lake City, Utah 84112, USA*
[5] *Centro de Astronomía, Universidad de Antofagasta, Avenida Angamos 601, Antofagasta 1270300, Chile*
[6] *Department of Physics and Astronomy, University of Pittsburgh, 3941 O'Hara Street, Pittsburgh, Pennsylvania 15260, USA*
[7] *Apache Point Observatory, P.O. Box 59, Sunspot, New Mexico 88349, USA*
[8] *McDonald Observatory, The University of Texas at Austin, 1 University Station, Austin, Texas 78712, USA*

Accepted XXX. Received YYY; in original form ZZZ

ABSTRACT

Dust attenuation in star-forming spiral galaxies affects stars and gas in different ways due to local variations in dust geometry. We present spatially resolved measurements of dust attenuation for a sample of 232 such star-forming spiral galaxies, derived from spectra acquired by the SDSS-IV MaNGA survey. The dust attenuation affecting the stellar populations of these galaxies (obtained using full spectrum stellar population fitting methods) is compared with the dust attenuation in the gas (derived from the Balmer decrement). Both of these attenuation measures increase for local regions of galaxies with higher star formation rates; the dust attenuation affecting the stellar populations increases more so than the dust attenuation in the gas, causing the ratio of the dust attenuation affecting the stellar populations to the dust attenuation in the gas to decrease for local regions of galaxies with higher star formation rate densities. No systematic difference is discernible in any of these dust attenuation quantities between the spiral arm and inter-arm regions of the galaxies. While both the dust attenuation in the gas and the dust attenuation affecting the stellar populations decrease with galactocentric radius, the ratio of the two quantities does not vary with radius. This ratio does, however, decrease systematically as the stellar mass of the galaxy increases. Analysis of the radial profiles of the two dust attenuation measures suggests that there is a disproportionately high concentration of birth clouds (incorporating gas, young stars and clumpy dust) nearer to the centres of star-forming spiral galaxies.

Key words: galaxies: spiral – ISM: dust – ISM: extinction – galaxies: star formation

1 INTRODUCTION

Properties of galaxies such as gas metallicities and star formation rates (SFRs) are derived from nebular emission lines produced as a result of gas heated by star-forming (SF) regions. However, this light at optical and ultraviolet (UV) wavelengths is absorbed and scattered by dust between the emission source and the observer, which results in dust attenuation.[1] We refer the reader to Kewley et al. (2019) and Salim & Narayanan (2020) for recent reviews on emission lines and dust attenuation respectively, and Calzetti (2001) for a pioneering study on dust within star-forming galaxies.

[1] *Extinction* is defined as absorption + scattering by dust grains out of the observer's line of sight. This phenomenon is not to be confused with *attenuation*, which is absorption + scattering into and out of the observer's line of sight. These terms are often erroneously used interchangeably – see Fig. 1 of Salim & Narayanan (2020) for further clarification.

★ E-mail: michael.greener@nottingham.ac.uk

Downloaded from https://academic.oup.com/mnras/advance-article-abstract/doi/10.1093/mnras/staa1300/5838054 by guest on 18 May 2020

SF spiral galaxies are undergoing dynamical and structural evolution (see reviews in Boselli & Gavazzi 2006 and Sánchez 2019), and are often associated with regions with considerable SFRs (e.g. Roberts 1969; Kennicutt 1998; Boselli & Gavazzi 2006; Sánchez 2019). These findings are of particular interest for this work, as SFRs are often correlated with the total dust content of SF galaxies (e.g. Da Cunha et al. 2008, 2010; Rowlands et al. 2014; Rémy-Ruyer et al. 2015).

Models of dust attenuation usually consider two main components in spiral galaxies: (1) *an interstellar medium (ISM)*, which is diffuse and increases in density closer to the galactic centre (e.g. Peletier et al. 1995; Boissier et al. 2004; Muñoz-Mateos et al. 2009; Wild et al. 2011; González Delgado et al. 2015; Goddard et al. 2016); and (2) *birth clouds (BCs)*, in which dust is very highly concentrated, clumpy, and therefore optically thicker than the ISM (e.g. Lonsdale Persson & Helou 1987; Charlot & Fall 2000; Calzetti 2001; Wild et al. 2011; Wuyts et al. 2013; Price et al. 2014). While all stars are born within these dense clouds, stellar migration means that only the youngest, hottest and most massive O and B stars remain in close proximity to their BCs (e.g. Walborn et al. 1999; Sellwood & Binney 2002; Roškar et al. 2008; Minchev & Famaey 2009; Loebman et al. 2010; Frankel et al. 2018; Minchev et al. 2018; Feltzing et al. 2020). These massive, young stars then ionise the surrounding gas, forming H II regions within the BCs. The central SF region is surrounded by clumps of gas and dust – propelled outwards by outflows from the starburst site – which absorb both continuum photons and those from the H II regions alike (Charlot & Fall 2000; Calzetti 2001).

We ultimately want to better understand the nature of dust attenuation, and how it affects astronomical observations. The motivation for doing so is compelling. The dust content of galaxies has been shown to correlate with their gas metallicities and gas contents (Calzetti 2001), but its presence reduces and reddens both the UV and optical flux emerging from host galaxies. This effect results in biased measurements of SFRs (Madau et al. 1996; Steidel et al. 1999; Glazebrook et al. 1999; Sullivan et al. 2000; Bell & Kennicutt 2001; Da Cunha et al. 2010), SFRs per unit physical surface area (Buat et al. 1989; Kennicutt et al. 2007; Li et al. 2019), SFR densities (Brinchmann et al. 2004), specific SFRs (Buat et al. 2006; Pannella et al. 2009), gas metallicities (Gilbank et al. 2010; Wilkinson et al. 2015), mass and luminosity densities (Brinchmann et al. 2004; Driver et al. 2007), and even distance estimates (Giovanelli et al. 1995).

Previous authors (e.g. Fanelli et al. 1988; Storchi-Bergmann et al. 1994; Calzetti et al. 1994, 2000; Kreckel et al. 2013) have extensively quantified and compared two independent measures of dust attenuation. Firstly, measurements of the the ratio of the Balmer emission lines Hα to Hβ are used as a diagnostic to derive the dust attenuation in the gas. The ratio of Hα to Hβ is known as the Balmer decrement. Since both lines are produced by the recombination of gas ionised by young stars, the Balmer decrement provides a measure of the dust attenuation due to the clumpy BCs, and so is useful to map the distribution of these dust clumps within the SF galaxies. The second measure is of the dust attenuation affecting the stellar populations. The gas is associated with the young stars close to the plane of the host galaxies, where dust is concentrated; the stars, by contrast, have a much greater scaleheight on average. Furthermore, since the dust and gas are well-mixed, we therefore might expect the dust attenuation in the gas to be higher than that affecting the stellar populations. Previous work, in which the ratio of these two dust attenuation measures has been calculated, has determined that this is indeed the case (e.g. Fanelli et al. 1988; Storchi-Bergmann et al. 1994; Calzetti et al. 1994, 2000; Kreckel et al. 2013).

The measurements made by many of these previous authors, are, however, limited by the lack of spatial resolution. Fortunately, integral field spectroscopic surveys, such as the Calar Alto Legacy Integral Field Area (CALIFA; Sánchez et al. 2012) survey, the Multi Unit Spectroscopic Explorer Wide (MUSE-Wide; Urrutia et al. 2019) survey, and the largest such survey, Mapping Nearby Galaxies at Apache Point Observatory (MaNGA; Bundy et al. 2015), now allow for spatially resolved observations of nearby spiral galaxies with a representative range of masses and SFRs. Such observations provide spatially resolved measurements for each of the dust attenuation derived from the gas, the dust attenuation affecting the stellar populations, and the excess between the former quantity and the latter. This final metric is perhaps a more physically meaningful property than the ratio between the two dust attenuation measures determined by previous studies, since it quantifies the excess dust attenuation close to the plane of the galaxy.

In this work, we quantify the dust attenuation in a well-defined sample of 232 nearby SF spiral galaxies with the aid of integral field spectroscopy. Two independent, but complementary, methods are used: first by using the Balmer decrement as a diagnostic for the dust attenuation in the gas, and second by using full-spectrum stellar population fitting methods to measure the dust attenuation affecting the stellar populations in the same galaxies.

We will use this analysis to propose a new geometry for the dust distribution in SF spiral galaxies, as well as putting better constraints on the difference between the optical depth of the Balmer emission lines Hα and Hβ and that affecting the stellar continuum. It is relatively easy to use measurements of the Balmer decrement to determine the dust attenuation in low-redshift galaxies (e.g. Sullivan et al. 2000; Bell & Kennicutt 2001; Kreckel et al. 2013) and in high-redshift galaxies (e.g. Glazebrook et al. 1999). For low-redshift galaxies, while the attenuation affecting the stellar populations can also be readily measured (e.g. Sullivan et al. 2000; Kreckel et al. 2013), this technique becomes increasingly difficult for more distant galaxies (e.g. Madau et al. 1996). A robust conversion factor between the two dust attenuation measures, such as is calculated in this work, is therefore an invaluable tool for observing distant galaxies.

The paper is structured as follows. Section 2 outlines technical details of the MaNGA survey, the Galaxy Zoo:3D project, and steps taken during data reduction and analysis. Section 3 describes the methods implemented to quantify dust attenuation. In Section 4 we present the results and subsequent discussion of this work, and compare the differences between looking globally and locally at the same data. Finally, we propose a new geometry for dust in spiral galaxies in Section 5 and draw our conclusions in Section 6.

Throughout this paper, we employ a Chabrier (2003) initial mass function (IMF). Luminosities, masses, and SFRs

Downloaded from https://academic.oup.com/mnras/advance-article-abstract/doi/10.1093/mnras/staa1300/5838054 by guest on 18 May 2020

are calculated assuming a ΛCDM cosmology with $\Omega_M = 0.3$, $\Omega_\Lambda = 0.7$, and $H_0 = 70\,\mathrm{km\ s^{-1}\ Mpc^{-1}}$.

2 OBSERVATIONS AND DATA

2.1 The MaNGA Survey

The MaNGA galaxy survey (Bundy et al. 2015) is part of the fourth generation of the Sloan Digital Sky Survey (SDSS-IV; Blanton et al. 2017), and will survey over 10 000 nearby galaxies by 2020 (Yan et al. 2016b; Wake et al. 2017). It uses Integral Field Unit (IFU) spectroscopy to obtain detailed spectral information about these galaxies. Hexagonal arrangements of IFU fibres are used to obtain spatial coverage to a distance of 1.5 and 2.5 effective radii (R_e) for the primary and secondary samples respectively (Law et al. 2015). Each fibre bundle is connected to a multi-object fibre spectrograph (Smee et al. 2013; Drory et al. 2015) attached to the 2.5 m telescope at Apache Point Observatory (APO; Gunn et al. 2006). MaNGA has a wavelength range of 3600 – 10300 Å, and a spectral resolution of $R \sim 2000$ (Bundy et al. 2015). The result is high-quality optical spectroscopy across the face of a large sample of low-redshift galaxies.

Raw data from MaNGA are calibrated (Yan et al. 2016a) and reduced by the Data Reduction Pipeline (DRP; Law et al. 2016); spectral indices and stellar and gas properties of the galaxies, such as the Gaussian profile integrated emission line fluxes, used in this work are made available thanks to the Data Analysis Pipeline (DAP; Westfall et al. 2019; Belfiore et al. 2019). DAP products may be accessed, inspected, and downloaded using the Python package and web application `Marvin` (Cherinka et al. 2018). Prior to analysis, the DAP subtracts the stellar spectrum from the emission lines of each MaNGA spaxel, correcting for stellar absorption and providing purely the emission due to the gas. The DAP also accounts for the Milky Way reddening using the O'Donnell (1994) reddening law.

The MaNGA sample is inherently mass-biased: high-mass galaxies are over-represented and low-mass galaxies are under-represented in the sample, in order to obtain similar numbers of galaxies in all mass ranges. In certain circumstances, such as when average global quantities for the sample are calculated in this work, it is necessary to correct for this bias to ensure that the sample is representative of the Universe as a whole. This correction is achieved via the use of the DRP `esweights` to statistically convert the sample into a volume-limited, mass-complete one. We refer to this correction throughout this work as "volume-weighting".

Galactocentric radius values used in this work are normalised by the elliptical Petrosian effective radius (a measure of the half-light radius), based on the SDSS *r*-band, from the NASA Sloan Atlas (NSA; Blanton et al. 2005, 2011) catalogue. This method is the most reliable way to measure photometric properties of MaNGA galaxies, and is done in order to account for the effects of inclination on radius measurements. Similarly, stellar mass estimates are taken from the NSA catalogue, again derived from elliptical Petrosian photometry; these masses are produced using `KCORRECT` (Blanton & Roweis 2006), and assuming a Chabrier (2003) IMF. See Fraser-McKelvie et al. (2019) for an in-depth discussion on obtaining stellar mass estimates for SDSS galaxies.

2.2 Sample Selection using Galaxy Zoo:3D

We analyse only spiral galaxies in this work for several reasons. Firstly, sample selection based purely on SFR or colour could select very different physical systems. However, studying only disk galaxies and excluding irregular galaxies from our analysis means that the distribution of stars, gas and dust within the galaxies is more regular, with a clearly defined disk and spiral arms. Furthermore, we also wanted to test whether dust attenuation properties between the spiral arm and inter-arm regions of the galaxies exhibit any differences.

Since we are endeavouring to analyse a well-defined sample of unequivocally spiral galaxies, we choose a subset of 253 galaxies classified as spirals by Galaxy Zoo:3D (GZ:3D; Masters et al., *in prep.*), which are drawn from the primary and secondary samples of the eighth MaNGA Product Launch (MPL-8) data release.[2] GZ:3D is a citizen science project in which volunteers identify the spiral arms and bars of MaNGA galaxies using a freehand drawing tool, which people use to decide how best to enclose the spiral arms of galaxies in SDSS images. Each person effectively 'votes' on the MaNGA spaxels which they consider to be part of the spiral arms. The result is a mask for the 253 spiral galaxies: spaxels with a greater number of votes are weighted accordingly and are likely to comprise part of the spiral arms of the galaxies.

Selecting only the GZ:3D spirals has two further advantages. First, almost all GZ:3D spirals are close to face-on, as a result of volunteers determining the location of spiral arms more readily in face-on galaxies than in edge-on galaxies. Consequently, it is easier to consistently compare dust attenuation properties of different galaxies within this sample, since the variation of inclination from galaxy to galaxy is small. Moreover, choosing purely GZ:3D spirals ensures that each galaxy has well-defined spiral arms, reducing ambiguity in subsequent analysis.

We excluded any galaxies with DAP datacube quality flags cautioning "do not use", or with two or more "warning" flags, which reduced the sample to 247 galaxies. Finally, to ensure that the individual spaxels used for analysis in this work were of a sufficiently high quality, a minimum continuum signal to noise (S/N) cut of 10 or higher was imposed; spaxels below this threshold were discarded prior to analysis.

2.3 BPT Diagrams

The Balmer decrement is only a valid measure of the dust attenuation due to the clumpy BCs associated with the youngest stellar populations if the Hα and Hβ emission lines for a given spaxel are actually produced by the recombination of gas ionised by these stars. This is because the adopted intrinsic value of the ratio of the Hα emission line to the Hβ line is dependent on the emission being produced by photoionisation. We therefore analyse only regions of the galaxies that are dominated by SF processes, and exclude regions for which active galactic nuclei (AGN) – and other

[2] Although we here use data from MPL-8, the GZ:3D sample was originally a subset of the MPL-5 spirals which more than 50% of respondents to the Galaxy Zoo 2 (GZ2; Willett et al. 2013; Hart et al. 2016) project marked as having either spiral arms or a bar.

Downloaded from https://academic.oup.com/mnras/advance-article-abstract/doi/10.1093/mnras/staa1300/5838054 by guest on 18 May 2020

excitation mechanisms – are responsible for the majority of the line emission. To this end, we employ the most commonly used Baldwin, Phillips and Terlevich (BPT; Baldwin et al. 1981; see also Veilleux & Osterbrock 1987) diagram. This diagnostic compares the line ratio [O III] λ5007/Hβ to [N II] λ6583/Hα. We therefore excluded galaxies which only had Hα, Hβ, [O III] λ5007 or [N II] λ6583 signal data for < 5% of their spaxels, which reduced the sample yet further to 232 galaxies. Furthermore, individual spaxels lacking signal data for any of the above emission lines were also rejected.

This analysis follows the work of Belfiore et al. (2015, 2016), who also provide an overview of BPT diagrams in their work. The line ratios described above are particularly useful for this work because they have similar wavelengths, and so will not be affected much by the dust that we are endeavouring to measure. The exact demarcation between SF and non-SF regions is not uniquely defined; in this work, we follow the method outlined by Belfiore et al. (2016) for applying BPT diagrams to MaNGA galaxies and consider line emission in spaxels below the less stringent Kewley et al. (2001) demarcation line to be dominated by SF regions. Consequently, spaxels in the 'composite' region between the demarcation lines of Kewley et al. (2001) and Kauffmann et al. (2003) are classified as SF in this work. Spaxels above the Kauffmann et al. (2003) line are assumed to be dominated by excitation mechanisms that are not SF in nature – such as AGN, Low Ionisation (Nuclear) Emission line Regions (LI(N)ERs), shocks and Seyfert galaxies – and are thus discarded prior to analysis. In total, the final sample used in this work comprises almost 140000 spaxels, belonging to 232 SF spiral galaxies out of the original 253 GZ:3D galaxies.

3 MEASURES OF DUST ATTENUATION

3.1 Measuring Dust Attenuation from Emission Line Ratios

The amount of dust attenuation along a given line of sight may be inferred by measuring the ratio of the Hα emission line to the Hβ line of the spectrum concerned. This ratio, known as the Balmer decrement, is fundamentally determined both by quantum mechanics and the physical conditions of the gas (namely its electron temperature and electron density). Any measured deviation from its intrinsic value can therefore be attributed to dust attenuation for a given electron temperature and electron density, assuming Case B recombination (Osterbrock & Ferland 2005). See Groves et al. (2012) for a comprehensive discussion on the Balmer decrement pertaining to SDSS galaxies.

Ultimately, we want to produce Balmer-decrement derived dust attenuation maps for the sample of galaxies, as well as Balmer-decrement corrected SFR maps, so that we can categorise spaxels by SFR per unit physical surface area. As described in Section 2.1, the initial processing of MaNGA data by the DAP has already corrected the emission line fluxes for Milky Way reddening and absorption in the underlying stellar spectrum. Therefore, we need only correct for the dust attenuation intrinsic to the galaxies we are analysing. We first calculate the colour excess $E(B-V)$ using the equation from Osterbrock & Ferland (2005), as in Domínguez et al. (2013); Kreckel et al. (2013):

$$E(B-V) = 1.97 \log_{10}\left[\frac{(\mathrm{H}\alpha/\mathrm{H}\beta)_{\mathrm{obs}}}{2.87}\right]. \quad (1)$$

Equation (1) assumes an intrinsic value for $(\mathrm{H}\alpha/\mathrm{H}\beta)_{\mathrm{int}} = 2.87$, which is valid for an electron temperature, T_{e}, of $T_{\mathrm{e}} = 10^4$ K and an electron density, n_{e}, of $n_{\mathrm{e}} = 10^2$ cm^{-3}, under Case B recombination conditions (Osterbrock & Ferland 2005).

$(\mathrm{H}\alpha/\mathrm{H}\beta)_{\mathrm{int}}$ is not constant within galaxies; it is dependent upon both the local electron temperature and density. However, as discussed in Section 2.3, we only analyse those regions of the galaxies for which SF is the dominant source of line emission. In these regions, Osterbrock & Ferland (2005) find that at constant $n_{\mathrm{e}} = 10^2$ cm^{-3}, $(\mathrm{H}\alpha/\mathrm{H}\beta)_{\mathrm{int}}$ varies between 3.05 for an electron temperature of $T_{\mathrm{e}} = 5 \times 10^3$ K, and 2.76 for $T_{\mathrm{e}} = 2 \times 10^4$ K. The dependence on electron density is weaker: at constant $T_{\mathrm{e}} = 10^4$ K, $(\mathrm{H}\alpha/\mathrm{H}\beta)_{\mathrm{int}}$ falls only to 2.85 at $n_{\mathrm{e}} = 10^4$ cm^{-3}, and to 2.81 at $n_{\mathrm{e}} = 10^6$ cm^{-3} (Osterbrock & Ferland 2005). Altering the value of $(\mathrm{H}\alpha/\mathrm{H}\beta)_{\mathrm{int}}$ between these extreme values of 3.05 and 2.76 results in an uncertainty in $E(B-V)$ of less than 0.1. Since such a variation is negligible for the analysis in this work, we therefore assume that each spaxel has a uniform value of $(\mathrm{H}\alpha/\mathrm{H}\beta)_{\mathrm{int}} = 2.87$.

The ratio of the dust attenuation at some wavelength λ, A_λ, to the colour excess is denoted $R_\lambda = A_\lambda/E(B-V)$, and is determined at that wavelength for a given reddening curve. In this work, we adopt the reddening curve of Calzetti et al. (2000). When deriving the dust attenuation in the gas from measurements of the Balmer decrement, we choose $R_V = 3.1$; when measuring the dust attenuation affecting the stellar populations, however, we choose $R_V = 4.05$. For a detailed explanation as to why different R_V values are used to determine the two attenuation measures, we refer the reader to Calzetti et al. (2000); see also Catalán-Torrecilla et al. (2015); Pannella et al. (2015). For the gas, we thus obtain $A_{V,\,\mathrm{gas}} = 3.1E(B-V)$, and for the stellar populations, we instead have $A_{V,\,\mathrm{stars}} = 4.05E(B-V)$. In this way, the dust attenuation can be calculated purely from measurements of the emission line fluxes of Hα and Hβ for each SF spaxel within all galaxies in the sample.

3.2 Measuring Dust Attenuation from Stellar Population Modelling

We also determine an entirely independent measure of the dust attenuation affecting the stellar populations at each location on the galaxy. We use the full-spectrum stellar population fitting code `STARLIGHT` (Cid Fernandes et al. 2005) to derive a best-fit spectrum, created from a linear combination of a set of input single stellar population (SSP) template spectra – with no assumptions or restrictions on the shape of the derived star formation histories – and an applied dust attenuation. The fitting method used is similar to that used by Peterken et al. (2019), and is described fully by Peterken et al. (*in prep.*). Here we highlight the key relevant details.

Before fitting each spaxel's spectrum, emission lines are removed using the MaNGA DAP (Westfall et al. 2019; Belfiore et al. 2019). No binning of neighbouring spaxels is done, since we wish to fully retain all spatial information. Ge et al. (2018) show that `STARLIGHT` can be susceptible to

Downloaded from https://academic.oup.com/mnras/advance-article-abstract/doi/10.1093/mnras/staa1300/5838054 by guest on 18 May 2020

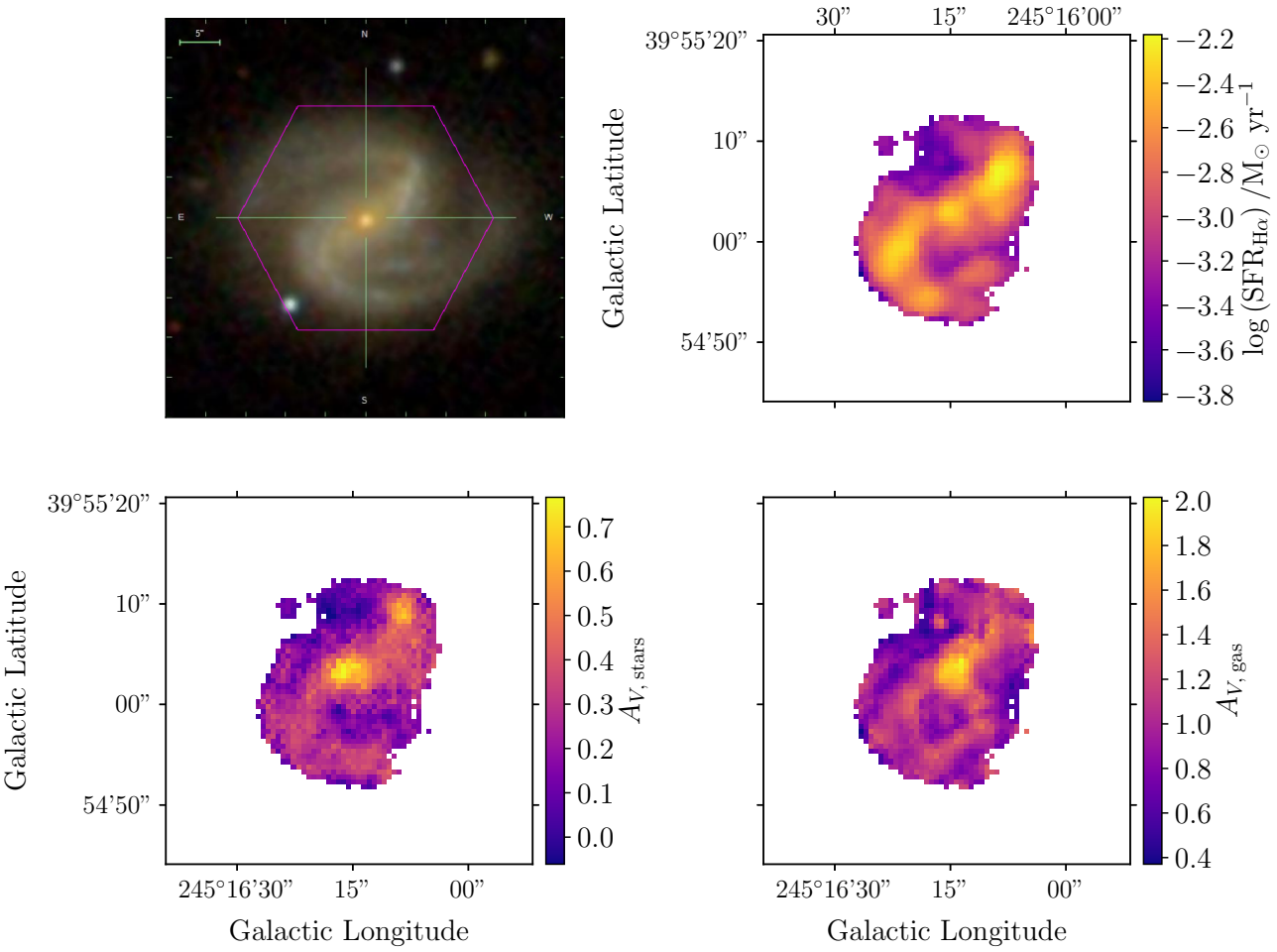

Figure 1. 3-colour SDSS image (top left), Balmer-decrement corrected SFR map (top right), dust attenuation map produced by `STARLIGHT` (bottom left), and dust attenuation map derived from the Balmer decrement (bottom right) for galaxy 8312-12702.

significant biases at low S/N, so we use the `STARLIGHT` configuration settings subsequently recommended by Cid Fernandes (2018), which prioritise robustness against such biases over computation times. 54 of the SSPs used are the E-MILES (Extended Medium-resolution Isaac Newton Telescope Library of Empirical Spectra) templates of Vazdekis et al. (2016), based on the earlier MILES library (Vazdekis et al. 2010). These templates cover a range of nine ages (in the range $7.85 \leq \log(\mathrm{age/yr}) \leq 10.25$) and six metallicities ($-1.71 \leq [\mathrm{M/H}] \leq +0.22$); they assume a Chabrier (2003) IMF, "Padova" isochrones (Girardi et al. 1999), and a Milky Way [α/Fe] ("baseFe"). As well as these E-MILES templates, we also include a further six ages (in the range $6.8 \leq \log(\mathrm{age/yr}) \leq 7.6$) and two metallicities ([M/H] = $-0.41, +0.00$) from the Asa'd et al. (2017) extension to the E-MILES library. These younger templates assume Bertelli et al. (1994) isochrones, and are very similar to those of Girardi et al. (1999) since they are also part of the Padova project; they are generated using the same method as the E-MILES SSP templates.

When building a best-fit spectrum from the SSPs, `STARLIGHT` also fits a dust attenuation $A_{V,\,\mathrm{stars}}$, for which a Calzetti et al. (2000) attenuation curve is assumed with an R_V of 4.05 (Calzetti et al. 2000; Catalán-Torrecilla et al. 2015; Pannella et al. 2015), as discussed in Section 3.1. The large wavelength range of the MaNGA and E-MILES spectra are exploited by fitting between 3541.4 and 8950.4 Å to use as much of the information contained in the whole continuum shape as possible to constrain the value of $A_{V,\,\mathrm{stars}}$. The value of $A_{V,\,\mathrm{stars}}$ is allowed to vary in the range $-1 \leq A_{V,\,\mathrm{stars}} \leq 8$ to allow for a full exploration of reasonable parameter space. The best fit results are, reassuringly, nearly all contained within the range $0 \leq A_{V,\,\mathrm{stars}} \leq 0.8$.

The `STARLIGHT` fit only applies a single $A_{V,\,\mathrm{stars}}$ to the overall spectrum. Such an approach is a simplification, since we expect the spectra of the youngest stellar populations to be attenuated to a greater degree than those of older populations. To allow for this discrepancy, `STARLIGHT` includes an option to include extra attenuation to be applied to specified SSP templates in the fit. However, in practice, the youngest

Downloaded from https://academic.oup.com/mnras/advance-article-abstract/doi/10.1093/mnras/staa1300/5838054 by guest on 18 May 2020

SSPs do not have strong spectral features, making this extra attenuation degenerate with changes in the continuum shape with population age or metallicity. We therefore do not use this feature. In addition, the contribution of the youngest stellar populations to the total spectrum is difficult to distinguish from the presence of hot stars present – but not modelled – in the oldest SSP templates which are responsible for the "UV upturn" (see Yi 2008 for a review). Peterken et al. (*in prep.*) show that this results in STARLIGHT fits which are unreliable for stellar populations younger than 30 Myr (an effect also found by Cid Fernandes & González Delgado 2009), but that the older populations are still modelled well.

Together, these limitations mean that the STARLIGHT attenuation measurements are liable to some uncertainties regarding the attenuation of the youngest stars. However, the value $A_{V,\,\mathrm{stars}}$ used in the fit is likely to be a good indicator of the average attenuation of the flux from the average stellar population. The stellar population effectively probed by STARLIGHT's attenuation measurement is significantly older than that probed using the Balmer decrement, which specifically measures the attenuation in the star-forming regions.

These $A_{V,\,\mathrm{stars}}$ measurements are determined for every SF spaxel in each of the sample galaxies. An example comparing the dust attenuation obtained in this way to that derived from measurements of the Balmer decrement (described in Section 3.1) for galaxy 8312-12702 is shown in Fig. 1.

4 LINKING DUST AND STAR FORMATION PROPERTIES

In order to understand whether variations in dust attenuation are driven primarily by global or local properties of galaxies, the data in this work are analysed on three different scales. Firstly, we categorise entire galaxies based on global quantities. We next take a more detailed look at the local quantities within these global categories by making use of the spatial resolution of MaNGA. Finally, we look yet more locally at the data, categorising spaxels rather than galaxies into different categories depending on local criteria.

4.1 Categorising Galaxies by Global Properties

We first present and discuss the results obtained from looking just at the global properties of the galaxies. In their seminal paper, Calzetti et al. (2000) found empirically that the global ratio of the reddening – i.e. the colour excess $E(B-V)$ – affecting the stellar continuum to that derived from the Balmer decrement was equal to 0.44 ± 0.03. Since the observed flux from the emission lines and the stellar continuum is not produced by the same stars, the attenuation of the former is more than twice as high as that of the latter (Keel 1993; Calzetti et al. 1994). The data of Calzetti et al. (2000) were obtained by the International Ultraviolet Explorer (IUE; Boggess et al. 1978). The IUE possessed both a high- and low-resolution spectrograph but was not equipped for integral field spectroscopy (Boggess et al. 1978). Therefore, we initially consider just the global properties of the galaxies in the sample; we do not (yet) make use of the spatial information that MaNGA provides for each galaxy.

Although our initial objective was simply to measure the value of this ratio obtained by these authors, we also

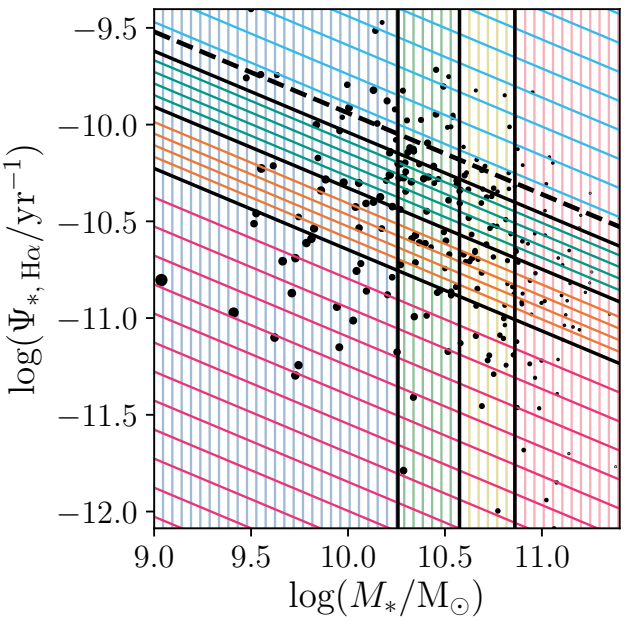

Figure 2. Specific SFR relative to the SF main sequence (dashed black line; Grootes et al. 2017) versus stellar mass for galaxies in the sample. Galaxies are first categorised based on their mass; we choose there to be roughly the same number of galaxies within each category. Galaxies in the blue region have stellar masses of $\log(M_*/\mathrm{M}_\odot) < 10.26$, those in the green have $10.26 < \log(M_*/\mathrm{M}_\odot) < 10.58$, those in the yellow have $10.58 < \log(M_*/\mathrm{M}_\odot) < 10.86$, and those in the red have $\log(M_*/\mathrm{M}_\odot) > 10.86$. We subsequently categorise galaxies by their vertical offset from the SFMS, $\Delta\log\left(\Psi_{*,\,\mathrm{H}\alpha}/\mathrm{yr}^{-1}\right)$: galaxies in the magenta region have a $\mathrm{sSFR}_{\mathrm{H}\alpha}$ of $\Delta\log\left(\Psi_{*,\,\mathrm{H}\alpha}/\mathrm{yr}^{-1}\right) < -0.71$ from the SFMS, those in the orange have $-0.71 < \Delta\log\left(\Psi_{*,\,\mathrm{H}\alpha}/\mathrm{yr}^{-1}\right) < -0.39$ from the SFMS, those in the teal have $-0.39 < \Delta\log\left(\Psi_{*,\,\mathrm{H}\alpha}/\mathrm{yr}^{-1}\right) < -0.10$ from the SFMS, and those in the cyan have $\Delta\log\left(\Psi_{*,\,\mathrm{H}\alpha}/\mathrm{yr}^{-1}\right) > -0.10$ from the SFMS. Solid black lines show the boundaries between these regions. The size of each point is directly proportional to the volume weight for each galaxy. Note that this plot does not show the total sSFRs of the galaxies: simply the sum of $\mathrm{SFR}_{\mathrm{H}\alpha}$ across all SF spaxels within each of the galaxies divided by the total stellar mass.

ultimately want to determine which galactic properties are the main drivers of variations in dust attenuation. Therefore, we choose to categorise the sample into four types by looking at two important global properties of galaxies (as shown in Fig. 2) – first their stellar mass, and second their specific SFR (sSFR; defined as SFR / stellar mass) relative to the star-forming main sequence (SFMS; Grootes et al. 2017). Of course, there are myriad SFMS calibrations from which to choose (for instance Noeske et al. 2007; Peng et al. 2010; Whitaker et al. 2012; Guo et al. 2015; Rodríguez del Pino et al. 2017 – and references within, notably Brinchmann et al. 2004 and Abazajian et al. 2009 – Spindler et al. 2017; Grootes et al. 2017; Salim et al. 2018). We employ the SFMS calculated by Grootes et al. (2017) since these authors fit a SFMS for spiral galaxies with redshifts of $z < 0.06$, which is the appropriate redshift range for the vast majority of the galaxies analysed in this work. Grootes et al. (2017)

Downloaded from https://academic.oup.com/mnras/advance-article-abstract/doi/10.1093/mnras/staa1300/5838054 by guest on 18 May 2020

derive SFRs by integrating the total near-UV luminosity of the galaxies in their sample.

In order to produce SFR maps for each of the galaxies, the intrinsic Hα flux $f_{\mathrm{int,\,H}\alpha}$ is determined for every SF spaxel in each of the galaxies in the sample:

$$f_{\mathrm{int,\,H}\alpha} = f_{\mathrm{obs,\,H}\alpha} \times 10^{0.4A_{\mathrm{H}\alpha}}, \tag{2}$$

where $f_{\mathrm{obs,\,H}\alpha}$ is the raw Hα flux from the DAP, and the Hα dust attenuation, $A_{\mathrm{H}\alpha} = 2.38E(B-V)$ for SF galaxies (using the Calzetti et al. 2000 reddening curve with $R_V = 3.1$). The Hα luminosity in Watts, $L_{\mathrm{H}\alpha}$ [W], of the galaxies is determined using the luminosity distances provided by the NSA catalogue (Blanton et al. 2005, 2011) for our chosen cosmology. The Hα derived SFR, $\mathrm{SFR}_{\mathrm{H}\alpha}$, for each SF spaxel in the galaxies may then be calculated using the Kennicutt (1998) relation, assuming a Chabrier (2003) IMF – see also Kreckel et al. (2013); Schaefer et al. (2017, 2018):

$$\mathrm{SFR}_{\mathrm{H}\alpha}\left[\mathrm{M}_\odot\ \mathrm{yr}^{-1}\right] = \frac{L_{\mathrm{H}\alpha}\ [\mathrm{W}]}{2.16\times10^{34}\ \mathrm{M}_\odot\ \mathrm{yr}^{-1}}. \tag{3}$$

A $\mathrm{SFR}_{\mathrm{H}\alpha}$ map produced in this way for one of the galaxies in the sample is shown in Fig. 1.

We first split the galaxies into four distinct categories based on their stellar masses (obtained from the NSA catalogue; Blanton et al. 2005, 2011), as seen in Fig. 2. These masses are also used in conjunction with the Hα derived SFRs calculated from Equation (3) to determine the global $\mathrm{sSFR}_{\mathrm{H}\alpha}$, $\Psi_{*,\,\mathrm{H}\alpha}$, for each galaxy. The galaxies are then additionally categorised by their vertical offset from the SFMS, $\Delta\log\left(\Psi_{*,\,\mathrm{H}\alpha}/\mathrm{yr}^{-1}\right)$ (shown in Fig. 2; Grootes et al. 2017); that is to say, galaxies are categorised by their $\mathrm{sSFR}_{\mathrm{H}\alpha}$ at a given mass. We choose not to categorise galaxies by $\mathrm{sSFR}_{\mathrm{H}\alpha}$ alone, since doing so would introduce bias due to the implicit dependence on stellar mass.

Figure 2 does not actually show the total sSFRs of the galaxies, since Balmer-decrement corrected SFRs can be calculated only for SF spaxels, as discussed in Section 2.3. Moreover, and of greater concern, the spatial coverage of MaNGA is limited to a distance of 1.5 R_{e} and 2.5 R_{e} for the galaxies in the primary and secondary samples, respectively. This means that we are at risk of calculating lower limits on the global Hα derived sSFRs of the sample galaxies. Nevertheless, the majority of star formation should still be captured, since it is likely to be enclosed within 1.5 R_{e}.

To estimate how much flux we typically miss in the outer regions of the galaxies, we compared global $\mathrm{SFR}_{\mathrm{H}\alpha}$ calculated from the primary and the secondary sample galaxies separately. The mean global $\mathrm{SFR}_{\mathrm{H}\alpha}$ for the primary sample galaxies is $1.5\pm0.1\mathrm{M}_\odot\ \mathrm{yr}^{-1}$, whereas the increased spatial coverage means that the mean global $\mathrm{SFR}_{\mathrm{H}\alpha}$ for the secondary sample galaxies is slightly higher, at $1.8\pm0.3\ \mathrm{M}_\odot\ \mathrm{yr}^{-1}$. It therefore seems likely that the limited MaNGA field of view means that the global Hα derived SFRs calculated in this work are systematically underestimated by ~20%. This can be seen in Fig. 2, in which many of the SF galaxies lie below the SFMS. It should be noted that this systematic effect does not compromise the final results of this work in any way, because we are interested only in analysing relative differences in star formation activity.

Figure 2 therefore plots the sum of the $\mathrm{SFR}_{\mathrm{H}\alpha}$ of each SF spaxel for each galaxy divided by the total stellar mass versus the total stellar mass of that galaxy. Bins are chosen such that there are roughly the same number of galaxies within each category. The lowest mass galaxies (blue) have stellar masses of $\log(M_*/\mathrm{M}_\odot) < 10.26$; the highest mass galaxies (red) have $\log(M_*/\mathrm{M}_\odot) > 10.86$. Galaxies with the lowest global Hα derived sSFRs relative to the SFMS (magenta) have a $\mathrm{sSFR}_{\mathrm{H}\alpha}$ of $\Delta\log\left(\Psi_{*,\,\mathrm{H}\alpha}/\mathrm{yr}^{-1}\right) < -0.71$ from the SFMS; those with the highest relative Hα derived sSFRs (cyan) have a $\mathrm{sSFR}_{\mathrm{H}\alpha}$ of $\Delta\log\left(\Psi_{*,\,\mathrm{H}\alpha}/\mathrm{yr}^{-1}\right) > -0.10$ from the SFMS. The definitions of these categories as outlined above are used when discussing the results of both Section 4.2 and Section 4.3.

4.2 Investigating the Impact of Global Effects on Dust Attenuation

Figure 3 shows the distributions of the global A_V dust attenuation affecting the stellar populations (hereafter denoted $A_{V,\,\mathrm{stars}}$), global A_V dust attenuation derived from the Balmer decrement (hereafter $A_{V,\,\mathrm{gas}}$), and the ratio of the two quantities (hereafter $A_{V,\,\mathrm{stars}}/A_{V,\,\mathrm{gas}}$) for each of the four stellar mass categories and the four categories of $\mathrm{sSFR}_{\mathrm{H}\alpha}$ relative to the SFMS. The average $A_{V,\,\mathrm{stars}}$ and $A_{V,\,\mathrm{gas}}$ values for each galaxy are light-weighted using the g-band flux. The histogram bins have been volume-weighted. Table 1 summarises the volume-weighted means of the light-weighted averages for the global $A_{V,\,\mathrm{stars}}$, $A_{V,\,\mathrm{gas}}$, and the ratio between the two quantities, for each of the four stellar mass categories and the four categories of $\mathrm{sSFR}_{\mathrm{H}\alpha}$ relative to the SFMS.

Both Fig. 3 and Table 1 show that $A_{V,\,\mathrm{gas}}$ consistently has a higher mean value than $A_{V,\,\mathrm{stars}}$. This finding is in agreement with the work of those who have extensively studied dust within starburst galaxies (e.g. Fanelli et al. 1988; Keel 1993; Calzetti et al. 1994, 2000; Kreckel et al. 2013). Both the peaks of the distributions in Fig. 3 and the mean global $A_{V,\,\mathrm{stars}}/A_{V,\,\mathrm{gas}}$ ratios in Table 1 may be compared with the value obtained by Calzetti et al. (2000), who found that $E(B-V)_{\mathrm{stars}}/E(B-V)_{\mathrm{gas}} = 0.44\pm0.03$. Accounting for the differing values of R_V used in the reddening curves for the stellar populations and the gas in this work (see Section 3.1), this ratio of colour excesses corresponds to a ratio of $A_{V,\,\mathrm{stars}}/A_{V,\,\mathrm{gas}} = 0.57\pm0.04$ (Calzetti et al. 2000). The ratios calculated in this work in Table 1 are systematically lower than that found by Calzetti et al. (2000).

The results in this work, however, should not be directly compared with those of Calzetti et al. (2000) for two main reasons. Firstly, the methods are different. Calzetti et al. (2000) derived the dust attenuation affecting the stellar populations by measuring the shape of the observed UV continuum; in this work, however, these attenuation values are obtained through the use of the full-spectrum stellar population synthesis code `STARLIGHT` (Cid Fernandes et al. 2005), which assumes a reddening curve for the stellar continuum. Secondly, the samples are different. The galaxies analysed by Calzetti et al. (2000) were starburst galaxies with exceptionally hyperactive SFRs: the mean and median SFRs of their galaxies are $18\pm5\,\mathrm{M}_\odot\ \mathrm{yr}^{-1}$ and $5\pm6\,\mathrm{M}_\odot\ \mathrm{yr}^{-1}$ respectively (Storchi-Bergmann et al. 1994). By contrast, the mean and median Hα derived SFRs of the MaNGA galaxies,

Downloaded from https://academic.oup.com/mnras/advance-article-abstract/doi/10.1093/mnras/staa1300/5838054 by guest on 18 May 2020

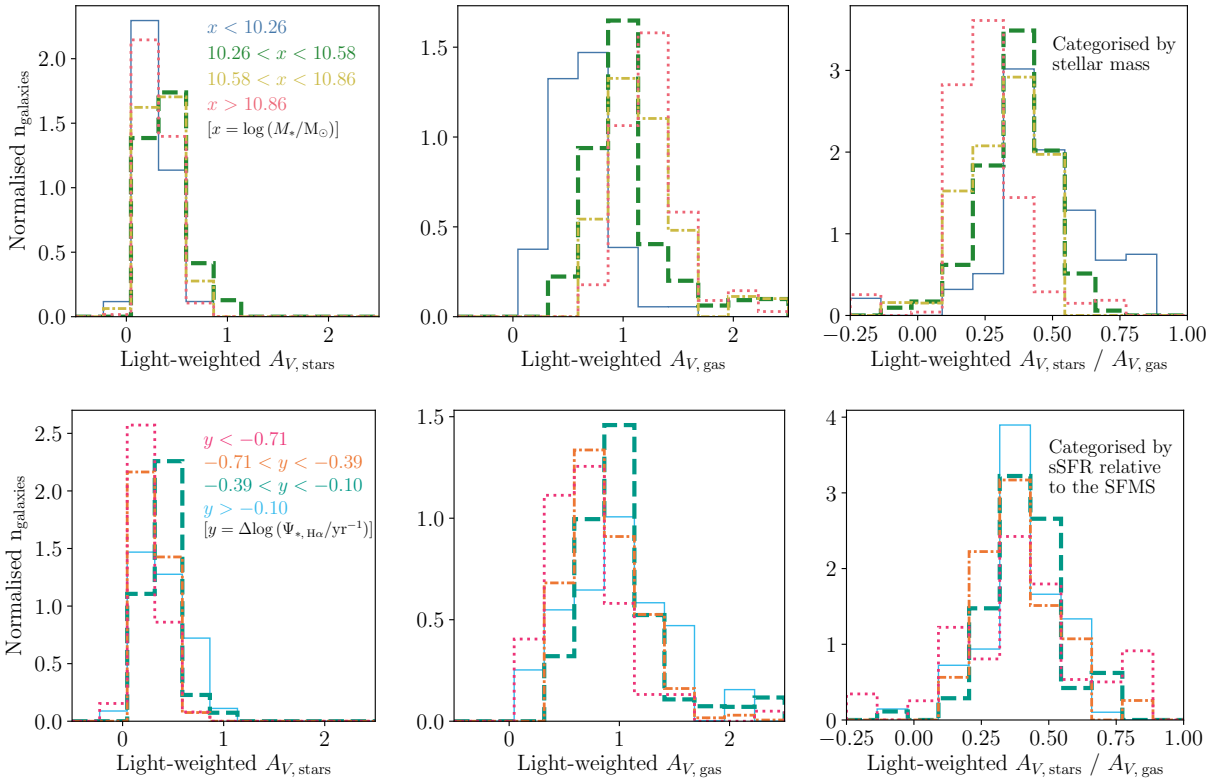

Figure 3. Distributions of (from left to right) light-weighted A_V dust attenuation affecting the stellar populations, light-weighted A_V dust attenuation derived from the Balmer decrement, and the ratio of the two quantities. The bins have been volume-weighted, and are normalised so that the area under each line is equal to one. Distributions on the top row have been categorised by stellar mass; blue lines denote the lowest-mass galaxies with stellar masses of $\log(M_*/\mathrm{M}_\odot) < 10.26$, green lines denote stellar masses of $10.26 < \log(M_*/\mathrm{M}_\odot) < 10.58$, yellow lines of $10.58 < \log(M_*/\mathrm{M}_\odot) < 10.86$, and red lines denote the highest-mass galaxies with stellar masses of $\log(M_*/\mathrm{M}_\odot) > 10.86$. Distributions on the bottom row have been categorised by global $\mathrm{sSFR}_{\mathrm{H}\alpha}$ relative to the SFMS; magenta lines denote that galaxies have a $\mathrm{sSFR}_{\mathrm{H}\alpha}$ of $\Delta\log\left(\Psi_{*,\,\mathrm{H}\alpha}/\mathrm{yr}^{-1}\right) < -0.71$ from the SFMS, orange lines denote a $\mathrm{sSFR}_{\mathrm{H}\alpha}$ of $-0.71 < \Delta\log\left(\Psi_{*,\,\mathrm{H}\alpha}/\mathrm{yr}^{-1}\right) < -0.39$ from the SFMS, teal lines denote a $\mathrm{sSFR}_{\mathrm{H}\alpha}$ of $-0.39 < \Delta\log\left(\Psi_{*,\,\mathrm{H}\alpha}/\mathrm{yr}^{-1}\right) < -0.10$ from the SFMS, and cyan lines denote a $\mathrm{sSFR}_{\mathrm{H}\alpha}$ of $\Delta\log\left(\Psi_{*,\,\mathrm{H}\alpha}/\mathrm{yr}^{-1}\right) > -0.10$ from the SFMS.

Table 1. Volume-weighted mean of the light-weighted averages of A_V dust attenuation affecting the stellar populations, A_V dust attenuation derived from the Balmer decrement, and the ratio of the two quantities, for galaxies categorised (1) by stellar mass; (2) by $\mathrm{sSFR}_{\mathrm{H}\alpha}$ relative to the SFMS, $\Delta\log\left(\Psi_{*,\,\mathrm{H}\alpha}/\mathrm{yr}^{-1}\right)$. The standard errors on the mean are quoted to 1σ. Also shown are the statistical significance levels between pairs of distributions in Fig. 3, determined via KS testing. Each sigma value corresponds to how significant the distinction is between a given distribution and the distribution in the table which immediately precedes it.

Stellar mass	Mean $A_{V,\,\mathrm{stars}}$		Mean $A_{V,\,\mathrm{gas}}$		Mean $A_{V,\,\mathrm{stars}}/A_{V,\,\mathrm{gas}}$	
	Value	Significance	Value	Significance	Value	Significance
$\log(M_*/\mathrm{M}_\odot) < 10.26$	0.27 ± 0.02	—	0.62 ± 0.03	—	0.43 ± 0.03	—
$10.26 < \log(M_*/\mathrm{M}_\odot) < 10.58$	0.36 ± 0.02	2.0σ	0.99 ± 0.04	$> 5\sigma$	0.36 ± 0.02	2.3σ
$10.58 < \log(M_*/\mathrm{M}_\odot) < 10.86$	0.33 ± 0.02	$< 1\sigma$	1.18 ± 0.05	3.4σ	0.29 ± 0.02	1.7σ
$\log(M_*/\mathrm{M}_\odot) > 10.86$	0.30 ± 0.02	$< 1\sigma$	1.20 ± 0.03	2.7σ	0.25 ± 0.01	2.9σ
$\mathrm{sSFR}_{\mathrm{H}\alpha}$ relative to the SFMS	Mean $A_{V,\,\mathrm{stars}}$		Mean $A_{V,\,\mathrm{gas}}$		Mean $A_{V,\,\mathrm{stars}}/A_{V,\,\mathrm{gas}}$	
	Value	Significance	Value	Significance	Value	Significance
$\Delta\log\left(\Psi_{*,\,\mathrm{H}\alpha}/\mathrm{yr}^{-1}\right) < -0.71$	0.25 ± 0.02	—	0.73 ± 0.05	—	0.41 ± 0.03	—
$-0.71 < \Delta\log\left(\Psi_{*,\,\mathrm{H}\alpha}/\mathrm{yr}^{-1}\right) < -0.39$	0.28 ± 0.02	$< 1\sigma$	0.83 ± 0.04	$< 1\sigma$	0.35 ± 0.02	$< 1\sigma$
$-0.39 < \Delta\log\left(\Psi_{*,\,\mathrm{H}\alpha}/\mathrm{yr}^{-1}\right) < -0.10$	0.37 ± 0.02	3.0σ	0.97 ± 0.05	$< 1\sigma$	0.39 ± 0.02	2.1σ
$\Delta\log\left(\Psi_{*,\,\mathrm{H}\alpha}/\mathrm{yr}^{-1}\right) > -0.10$	0.34 ± 0.03	3.7σ	0.92 ± 0.05	2.7σ	0.35 ± 0.03	2.0σ

Downloaded from https://academic.oup.com/mnras/advance-article-abstract/doi/10.1093/mnras/staa1300/5838054 by guest on 18 May 2020

at $1.6 \pm 0.1\,\mathrm{M}_\odot\,\mathrm{yr}^{-1}$ and $1.0 \pm 0.2\,\mathrm{M}_\odot\,\mathrm{yr}^{-1}$ respectively, are more representative of normal SF spiral galaxies.

We now consider the effect that both stellar mass and global $\mathrm{sSFR}_{\mathrm{H}\alpha}$ relative to the main sequence of SF galaxies have upon both of the dust attenuation measures, and the ratio between them.

Figure 3 shows that there is a dependence on the stellar mass of the galaxies for the global light-weighted $A_{V,\,\mathrm{gas}}$ and the $A_{V,\,\mathrm{stars}}/A_{V,\,\mathrm{gas}}$ ratio: the global light-weighted $A_{V,\,\mathrm{gas}}$ increases and the global light-weighted $A_{V,\,\mathrm{stars}}/A_{V,\,\mathrm{gas}}$ ratio decreases as the stellar mass of the galaxies increases. However, this effect is non-existent for the global light-weighted $A_{V,\,\mathrm{stars}}$, which remains roughly constant in each of the mass categories. Kolmogorov-Smirnov (KS) testing of the distributions in Fig. 3 reveals that the dependence on stellar mass for the global light-weighted $A_{V,\,\mathrm{gas}}$ and the $A_{V,\,\mathrm{stars}}/A_{V,\,\mathrm{gas}}$ ratio is statistically significant, but finds no statistical difference between the distributions in the global light-weighted $A_{V,\,\mathrm{stars}}$. The mean values of all of these quantities for each stellar mass category, as well as the significance levels to which the distributions are distinct, are summarised in Table 1.

Further KS testing of the distributions in Fig. 3 finds that there is only a weak dependence on global $\mathrm{sSFR}_{\mathrm{H}\alpha}$ relative to the SFMS for each of the global light-weighted $A_{V,\,\mathrm{stars}}$ and $A_{V,\,\mathrm{gas}}$: as the global $\mathrm{sSFR}_{\mathrm{H}\alpha}$ of the galaxies decreases relative to the SFMS, the values of both the attenuation measures decrease. No statistically significant dependence on global $\mathrm{sSFR}_{\mathrm{H}\alpha}$ relative to the SFMS is detected for the ratio of these two quantities; Table 1 shows that the mean values for the the global light-weighted $A_{V,\,\mathrm{stars}}/A_{V,\,\mathrm{gas}}$ ratio remain roughly constant at ~0.35.

4.3 Looking Locally within the Galaxies

We now use the spatial resolution of MaNGA to look not just at the global properties of the galaxies, but their local properties as well. In particular, we investigate how dust attenuation depends on the location within galaxies: how it varies spatially, with galactocentric radius, and between the spiral arm and inter-arm regions. Moreover, we study how these dust attenuation properties vary between the stellar mass and $\mathrm{sSFR}_{\mathrm{H}\alpha}$ categories defined in Section 4.1.

4.3.1 Dust Attenuation within Spiral Arms is not Resolved

Since dust lanes are often associated with the spiral arms of galaxies (e.g. Tamburro et al. 2008; Hou & Han 2015; Shabani et al. 2018), we use the GZ:3D spiral arm masks to decompose each of the galaxies in the sample into their spiral arm and inter-arm regions. Ultimately, however, almost no significant difference is seen between any of the dust attenuation quantities described so far for data inside the spiral arms and in the inter-arm regions. This null result is likely due to the relatively large FWHM of the MaNGA PSF of ~2.5" (Bundy et al. 2015); an angular distance of ~2 kpc at the average distance of the sample. At such a spatial resolution, the results are smeared and it is difficult to resolve whether dust lanes, which tend to be narrow (e.g Xilouris et al. 1999; Dalcanton et al. 2004; Holwerda et al. 2012), are located in the spiral arm or inter-arm region of the GZ:3D mask. This effect is compounded by the fact that GZ:3D respondents would naturally select the brightest part of the image as the spiral arm, which also is likely to exclude dust lanes which lag behind spiral arms (e.g. Egusa et al. 2004; Chandar et al. 2017) from the GZ:3D masks employed in this work. Finally, dust lanes are optically thick (e.g. White & Keel 1992; White et al. 2000; Holwerda et al. 2004), which will result in regions of reduced brightness, meaning they might be intentionally omitted from the GZ:3D masks.

4.3.2 Average and Radial Variation of Dust Attenuation: Dependence on Stellar Mass

We next investigate how the average dust attenuation quantities depend on galaxy stellar mass. Figure 4 shows graphs of each of local A_V dust attenuation affecting the stellar populations, local A_V dust attenuation derived from the Balmer decrement, and finally the ratio of, and the difference between, these two quantities as a function of radius. The blue points (far left column) are data from the lowest-mass galaxies in the sample. Moving rightwards, the stellar mass increases; the red data (far right column) are from the highest-mass galaxies in the sample. Volume-weighted running medians and inter-quartile ranges are overlaid on the data.

Figure 4 compares how the median local dust attenuation affecting the stellar populations, $A_{V,\,\mathrm{stars}}$, and the median local dust attenuation derived from measurements of the Balmer decrement, $A_{V,\,\mathrm{gas}}$, the ratio between the two attenuation measures, and the $A_{V,\,\mathrm{gas}}$ excess are affected by stellar mass. Of these quantities, the median local $A_{V,\,\mathrm{gas}}$ depends most strongly on stellar mass: its average value increases for increasing stellar mass. This finding is in agreement with those of other authors, who report higher average values for the local $A_{V,\,\mathrm{gas}}$ for higher-mass galaxies (Nelson et al. 2015a; Jafariyazani et al. 2019). By contrast, the median local $A_{V,\,\mathrm{stars}}$ does not change appreciably between each stellar mass category (although see González Delgado et al. 2015 and Goddard et al. 2016, both of whom do find higher average values for $A_{V,\,\mathrm{stars}}$ in galaxies with higher stellar masses. We likely do not see this effect since these authors had at their disposal a much wider range of stellar masses than in this work). At any rate, this work shows that the average value of $A_{V,\,\mathrm{gas}}$ is more strongly influenced by stellar mass than the average $A_{V,\,\mathrm{stars}}$; this in turn means that the average $A_{V,\,\mathrm{stars}}/A_{V,\,\mathrm{gas}}$ ratio decreases for increasing stellar mass.

So far, we have determined the $A_{V,\,\mathrm{stars}}/A_{V,\,\mathrm{gas}}$ ratio for the sake of comparison with the work of Calzetti et al. (2000). Although this ratio is a useful diagnostic for determining global properties of galaxies, it is actually not physically motivated, since A_λ is a logarithmic quantity measured in magnitudes (see for instance Salim & Narayanan 2020). Consequently, the ratio of $A_{V,\,\mathrm{stars}}$ to $A_{V,\,\mathrm{gas}}$ – a ratio of two logarithms – does not represent a physically meaningful quantity.

We therefore here introduce a new quantity, which we coin the $A_{V,\,\mathrm{gas}}$ excess, defined as $A_{V,\,\mathrm{gas}} - A_{V,\,\mathrm{stars}}$, and which unlike the $A_{V,\,\mathrm{stars}}/A_{V,\,\mathrm{gas}}$ ratio is physically motivated. Since (as we discuss in Section 3.2) `STARLIGHT` provides little information about the dust attenuation affecting the youngest stellar populations, $A_{V,\,\mathrm{stars}}$ primarily quantifies the contribution to the dust attenuation from the diffuse ISM. By contrast, $A_{V,\,\mathrm{gas}}$ quantifies the dust attenuation due to the combination of this diffuse ISM and the clumpy BCs. Therefore, by

Downloaded from https://academic.oup.com/mnras/advance-article-abstract/doi/10.1093/mnras/staa1300/5838054 by guest on 18 May 2020

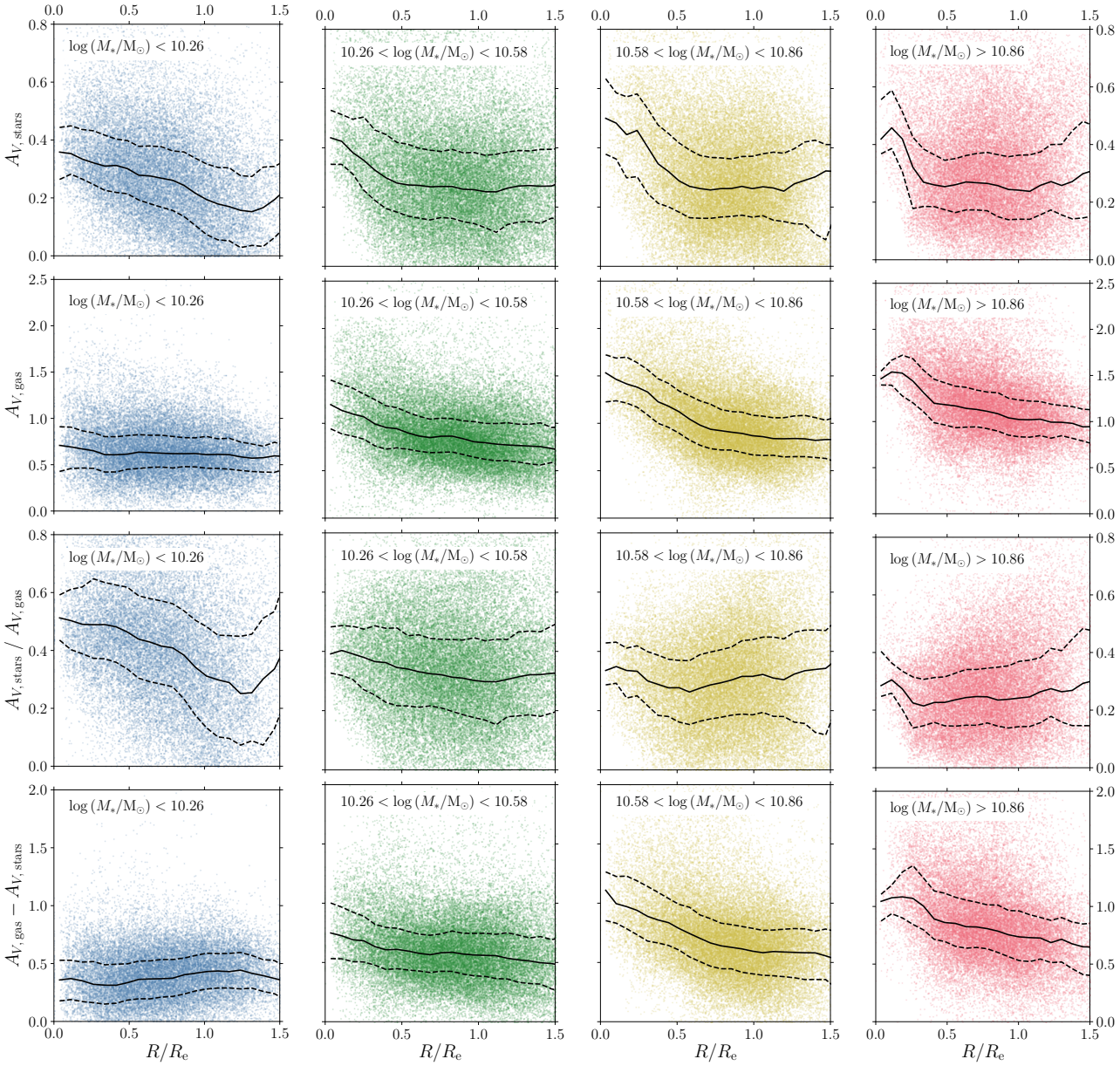

Figure 4. All spaxels plotted on scatter graphs showing the local A_V dust attenuation affecting the stellar populations (top row), the local A_V dust attenuation derived from the Balmer decrement (upper-middle row), the ratio of the two quantities (lower-middle row), and the difference between the two quantities (bottom row) as a function of distance from the galactic centre in units of R_e. The blue points (far left column) are data from galaxies with stellar masses in the range $\log(M_*/\mathrm{M}_\odot) < 10.26$, green (centre-left column) data are from galaxies with $10.26 < \log(M_*/\mathrm{M}_\odot) < 10.58$, yellow (centre-right column) data are from galaxies with $10.58 < \log(M_*/\mathrm{M}_\odot) < 10.86$, and the red (far right column) data from galaxies with $\log(M_*/\mathrm{M}_\odot) > 10.86$. The running medians (solid black lines) and inter-quartile ranges (dashed black lines) to the data have also been added to each plot. Each of these running averages have been volume-weighted.

subtracting $A_{V,\,\mathrm{stars}}$ from $A_{V,\,\mathrm{gas}}$ it is possible to estimate the dust attenuation *due the BCs alone*. Note that the $A_{V,\,\mathrm{gas}}$ excess probably over-estimates the dust attenuation due to the BCs, since `STARLIGHT` calculates the dust attenuation affecting the stellar populations down to $\sim 3\times10^7$yr, which are relatively young and will hence experience both attenuation from the diffuse ISM and their BCs.

Since measurements of the $A_{V,\,\mathrm{gas}}$ excess can also provide information about local variations in the dust geometry of SF galaxies, we now examine how the average of this newly-defined quantity varies with stellar mass. Figure 4 shows that a similar (though less pronounced) effect is seen in both the variation of the average $A_{V,\,\mathrm{gas}}$ excess and the average $A_{V,\,\mathrm{gas}}$, both of which increase as stellar mass increases.

As well as showing the average values of the dust attenuation quantities, Fig. 4 also shows that both the local $A_{V,\,\mathrm{stars}}$ and local $A_{V,\,\mathrm{gas}}$ exhibit some radial dependence: the inner regions possess higher values for both dust attenuation quantities, which flatten out beyond $\sim 0.5\ R_e$. Each stellar mass category sees the value of $A_{V,\,\mathrm{stars}}$ fall from around

Downloaded from https://academic.oup.com/mnras/advance-article-abstract/doi/10.1093/mnras/staa1300/5838054 by guest on 18 May 2020

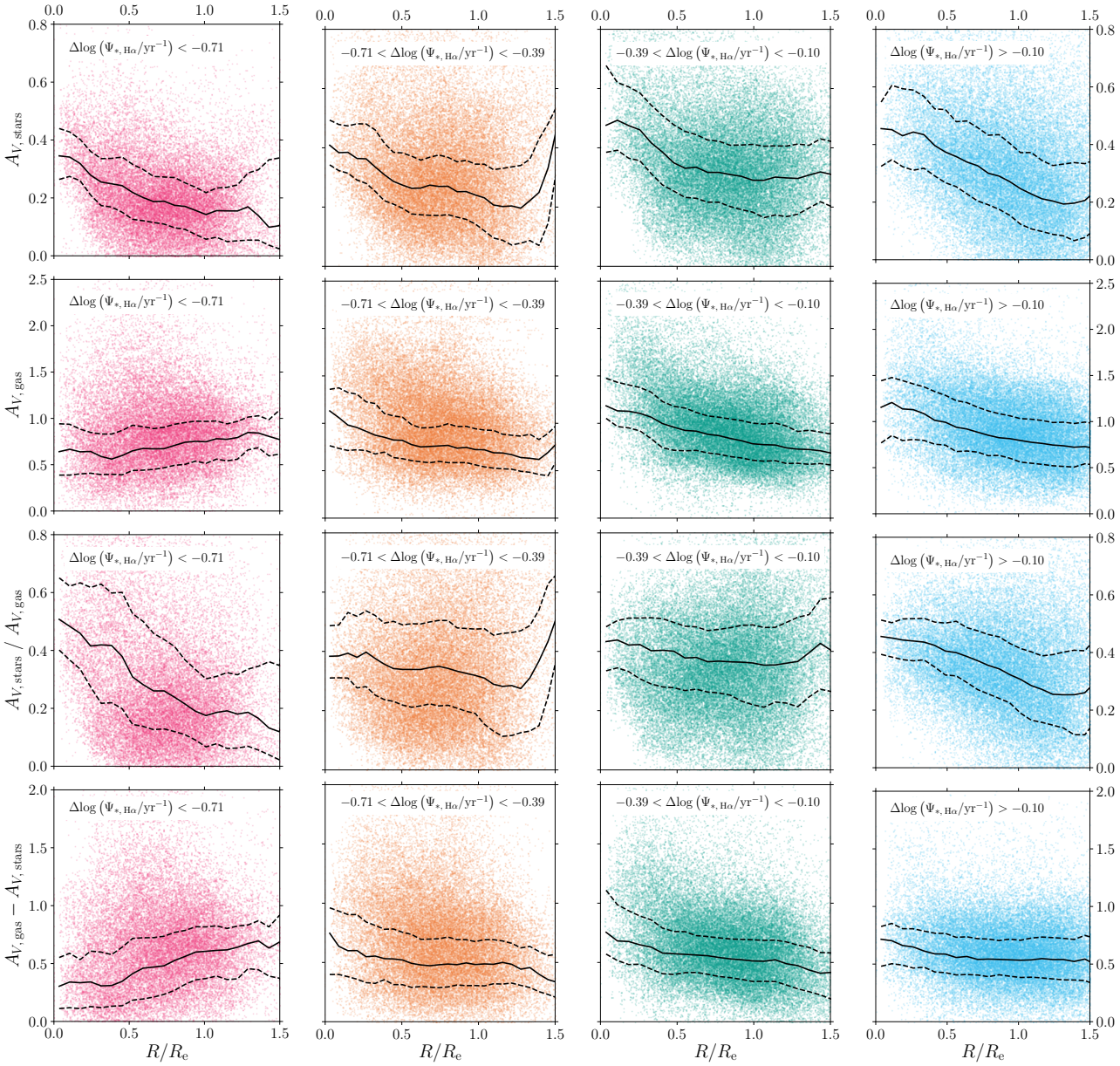

Figure 5. As in Fig. 4, except galaxies are now categorised by their global $\mathrm{sSFR}_{\mathrm{H}\alpha}$ relative to the SFMS. The magenta points (far left column) are data from galaxies with a $\mathrm{sSFR}_{\mathrm{H}\alpha}$ of $\Delta\log\left(\Psi_{*,\,\mathrm{H}\alpha}/\mathrm{yr}^{-1}\right) < -0.71$ from the SFMS, orange (centre-left column) data are from galaxies with a $\mathrm{sSFR}_{\mathrm{H}\alpha}$ of $-0.71 < \Delta\log\left(\Psi_{*,\,\mathrm{H}\alpha}/\mathrm{yr}^{-1}\right) < -0.39$ from the SFMS, teal (centre-right column) data are from galaxies with a $\mathrm{sSFR}_{\mathrm{H}\alpha}$ of $-0.39 < \Delta\log\left(\Psi_{*,\,\mathrm{H}\alpha}/\mathrm{yr}^{-1}\right) < -0.10$ from the SFMS, and the cyan (far right column) data are from galaxies with a $\mathrm{sSFR}_{\mathrm{H}\alpha}$ of $\Delta\log\left(\Psi_{*,\,\mathrm{H}\alpha}/\mathrm{yr}^{-1}\right) > -0.10$ from the SFMS.

$\sim$0.4 − 0.5 mag at the galactic centre to $\sim$0.2 − 0.3 mag at 1.5 R_{e}. Furthermore, the lowest-mass galaxies see no radial variation in their local $A_{V,\,\mathrm{gas}}$, which remains constant at around $\sim$0.6 mag, whereas for the highest-mass galaxies the local $A_{V,\,\mathrm{gas}}$ falls almost a magnitude from a value of $\sim$1.6 mag to $\sim$0.8 mag. It is tempting to explain away this lack of radial variation in the local $A_{V,\,\mathrm{gas}}$ for the lowest-mass galaxies by assuming that the bulges of low-mass galaxies are proportionally smaller than high-mass galaxies, thereby causing galaxies with lower stellar masses to exhibit lower values of local $A_{V,\,\mathrm{gas}}$ nearer to their central regions. However, analysis of the bulge-to-total (B/T) light ratio of each galaxy (see Simard et al. 2011) reveals that the mean B/T ratio is broadly similar for each category: this difference, therefore, is likely not a consequence of low-mass galaxies having small bulges in proportion to their size.

These findings are in agreement with previous work: both González Delgado et al. (2015) as well as Goddard et al. (2016) find that dust attenuation affecting the stellar populations exhibits a similar radial gradient for both CALIFA survey galaxies and MaNGA galaxies, respectively. Furthermore, both Nelson et al. (2015a) and Jafariyazani

Downloaded from https://academic.oup.com/mnras/advance-article-abstract/doi/10.1093/mnras/staa1300/5838054 by guest on 18 May 2020

et al. (2019) show that dust attenuation derived from measurements of the Balmer decrement declines radially in a very similar manner for both 3D-HST survey galaxies and MUSE-Wide survey galaxies, respectively. Moreover, these authors also report steeper radial gradients for higher-mass galaxies for both the local $A_{V,\,\mathrm{stars}}$ (González Delgado et al. 2015; Goddard et al. 2016) and for the local $A_{V,\,\mathrm{gas}}$ (Nelson et al. 2015a; Jafariyazani et al. 2019). Again, this behaviour can be seen in the plots of Fig. 4.

The local $A_{V,\,\mathrm{stars}}/A_{V,\,\mathrm{gas}}$ ratio is not particularly affected by radius at any galaxy stellar mass. The highest-mass galaxies (red) exhibit only a very small gradient close to their centres, after which $A_{V,\,\mathrm{stars}}/A_{V,\,\mathrm{gas}}$ remains reasonably constant with radius; the ratio for the intermediate-mass galaxies (yellow and green) is roughly constant between the galactic centre and 1.5 R_{e}. This behaviour is intriguing considering that $A_{V,\,\mathrm{stars}}$ and $A_{V,\,\mathrm{gas}}$ are independent measures of dust attenuation: to yield a ratio that is roughly constant with radius, both the local $A_{V,\,\mathrm{stars}}$ and $A_{V,\,\mathrm{gas}}$ must decrease with radius at approximately the same rate. The only exception is the local $A_{V,\,\mathrm{stars}}/A_{V,\,\mathrm{gas}}$ for the lowest-mass galaxies (blue), which exhibit a stronger radial gradient for this ratio, driven by the lack of such a gradient in the local $A_{V,\,\mathrm{gas}}$. Quite why the lowest-mass galaxies exhibit this behaviour is, however, unclear; it is possible that this could be a consequence of higher-mass galaxies having clumpier dust distributions and a greater amount of clumpy dust nearer to their centres than lower-mass galaxies.

The $A_{V,\,\mathrm{gas}}$ excess varies with radius in a very similar manner to the local $A_{V,\,\mathrm{gas}}$. The $A_{V,\,\mathrm{gas}}$ excess is higher at the centres of the galaxies than at their outskirts (again with the exception of those galaxies with the lowest stellar masses). This behaviour suggests that the radial gradients seen in the local $A_{V,\,\mathrm{gas}}$, both in this work and in other work (e.g. Nelson et al. 2015a; Jafariyazani et al. 2019) cannot be attributed to a radial gradient in the diffuse ISM alone.

4.3.3 Average and Radial Variation of Dust Attenuation: Dependence on Relative Global sSFR

When the same analysis is carried out based on the categories of relative global $\mathrm{sSFR}_{\mathrm{H}\alpha}$, similar results are obtained. These results are shown in Fig. 5, which plots each of the four dust attenuation quantities described in Section 4.3.2 as a function of radius. The magenta data (far left column) are from the galaxies with the lowest relative global Hα derived sSFRs. Moving rightwards, the relative global $\mathrm{sSFR}_{\mathrm{H}\alpha}$ increases; the cyan data (far right column) are from the galaxies with the highest relative global Hα derived sSFRs.

The median values of the local $A_{V,\,\mathrm{stars}}$, $A_{V,\,\mathrm{gas}}$, and the $A_{V,\,\mathrm{gas}}$ excess are less dependent on relative global $\mathrm{sSFR}_{\mathrm{H}\alpha}$ than stellar mass. Nevertheless, all of these attenuation quantities have higher values for galaxies with high relative global Hα derived sSFRs compared with those with low relative global Hα derived sSFRs. In contrast to the results of Fig. 4, the average $A_{V,\,\mathrm{stars}}/A_{V,\,\mathrm{gas}}$ ratio is not dependent on relative global $\mathrm{sSFR}_{\mathrm{H}\alpha}$; it has a constant median value of approximately ~0.35, since the average values of the local $A_{V,\,\mathrm{stars}}$ and $A_{V,\,\mathrm{gas}}$ are affected in very similar ways by the relative global $\mathrm{sSFR}_{\mathrm{H}\alpha}$ of the galaxy. This contrast suggests that stellar mass has more influence on the local dust attenuation properties of a galaxy than the relative global $\mathrm{sSFR}_{\mathrm{H}\alpha}$.

Strong radial gradients are found for the local $A_{V,\,\mathrm{stars}}$ for each of the four relative global $\mathrm{sSFR}_{\mathrm{H}\alpha}$ categories, as well as for the local $A_{V,\,\mathrm{gas}}$ for each of the categories (except the galaxies with the lowest relative global Hα derived sSFRs). The similar radial variation of these two independent measures of dust attenuation causes the local $A_{V,\,\mathrm{stars}}/A_{V,\,\mathrm{gas}}$ ratios to remain broadly constant between $0 - 1.5\ R_{\mathrm{e}}$ for each of the categories (except for galaxies with the lowest relative global Hα derived sSFRs). The radial gradients in the $A_{V,\,\mathrm{gas}}$ excess in Fig. 5, however, are not as strong as those seen in Fig. 4. While this behaviour again suggests that both the diffuse ISM and the clumpy BCs increase in density nearer to the centres of the galaxies (apart from those with the lowest relative global Hα derived sSFRs), it also reiterates that the galaxy stellar mass is a more important driver of local dust attenuation properties than the relative global $\mathrm{sSFR}_{\mathrm{H}\alpha}$.

4.4 Variations in Dust Attenuation Properties are Driven Predominantly by Local Physics

Having studied the effect of global galaxy properties on dust attenuation, we now consider the effect of local properties. The spatial resolution of MaNGA means that we do not have to group spaxels belonging to the same galaxies into the same categories: we can split the spaxels of each galaxy into multiple groups. In other words, the local effects of dust attenuation are now analysed, rather than purely global effects. Spaxels are categorised based on their $\mathrm{SFR}_{\mathrm{H}\alpha}$ per unit physical surface area (hereafter denoted $\Sigma_{\mathrm{SFR,\,H}\alpha}$), as seen in Fig. 6. The histogram bins have been volume-weighted.

We compare the effect of global $\mathrm{sSFR}_{\mathrm{H}\alpha}$ with local $\Sigma_{\mathrm{SFR,\,H}\alpha}$ rather than with local $\mathrm{sSFR}_{\mathrm{H}\alpha}$ since Σ_{SFR} is proportional to SFR per unit physical volume for disks of approximately uniform thickness. SFR per unit physical surface area is hence a more direct physical measurement of the star formation activity in a given region of a galaxy than SFR per unit stellar mass; moreover, local Σ_{SFR} is a less model-dependent measure of star formation activity than local sSFR and will still show similar results (e.g. González Delgado et al. 2016; Medling et al. 2018; Sánchez 2019).

Figure 7 shows the distributions of the local A_V dust attenuation affecting the stellar populations, local A_V dust attenuation derived from the Balmer decrement, the ratio of the two quantities, and the difference between the two quantities. The histogram bins have been volume-weighted. Table 2 summarises the mean values of the volume-weighted local $A_{V,\,\mathrm{stars}}$, the volume-weighted local $A_{V,\,\mathrm{gas}}$, and both the ratio and the difference between the two quantities for each of the four newly defined categories.

Figure 7 shows that there is a strong dependence on $\Sigma_{\mathrm{SFR,\,H}\alpha}$ for each of the local $A_{V,\,\mathrm{stars}}$, the local $A_{V,\,\mathrm{gas}}$, the ratio of these two quantities, and the local $A_{V,\,\mathrm{gas}}$ excess ($A_{V,\,\mathrm{gas}} - A_{V,\,\mathrm{stars}}$). KS tests confirm what can be seen by eye – each of the pairs of neighbouring distributions in Fig. 7 are found to be distinct to well over 5σ confidence. As the $\Sigma_{\mathrm{SFR,\,H}\alpha}$ of the spaxels increases, higher values are seen both for the dust attenuation affecting the stellar populations and the dust attenuation derived from measurements of the Balmer decrement. These trends are in agreement with previous work: SFR is shown to be strongly correlated with the total dust content of galaxies (e.g. Da Cunha et al. 2008,

Downloaded from https://academic.oup.com/mnras/advance-article-abstract/doi/10.1093/mnras/staa1300/5838054 by guest on 18 May 2020

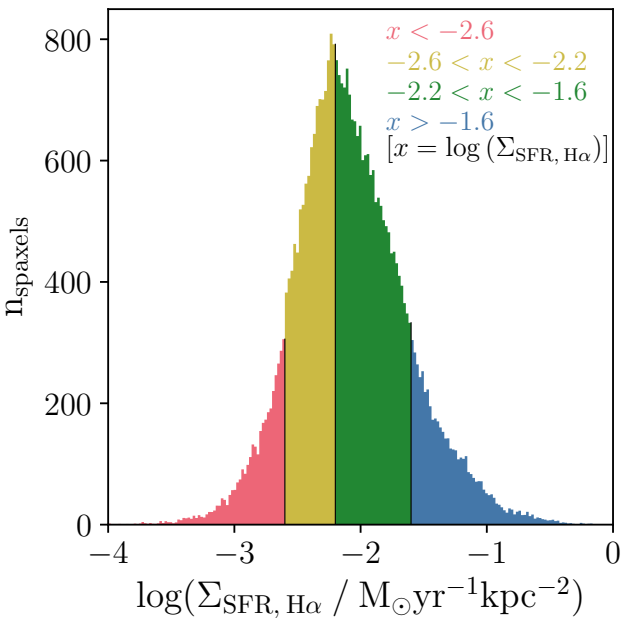

Figure 6. Histogram of all spaxels in the sample binned by $\mathrm{SFR_{H\alpha}}$ per unit physical surface area, $\Sigma_{\mathrm{SFR,\,H\alpha}}$. The bins have been volume-weighted. The red region contains spaxels with the lowest $\Sigma_{\mathrm{SFR,\,H\alpha}}$, with $\log(\Sigma_{\mathrm{SFR,\,H\alpha}}\ /\ \mathrm{M_\odot\ yr^{-1}\ kpc^{-2}}) < -2.6$; yellow contains $-2.6 < \log(\Sigma_{\mathrm{SFR,\,H\alpha}}\ /\ \mathrm{M_\odot\ yr^{-1}\ kpc^{-2}}) < -2.2$; green contains $-2.2 < \log(\Sigma_{\mathrm{SFR,\,H\alpha}}\ /\ \mathrm{M_\odot\ yr^{-1}\ kpc^{-2}}) < -1.6$; and the blue region contains spaxels with the highest $\Sigma_{\mathrm{SFR,\,H\alpha}}$, with $\log(\Sigma_{\mathrm{SFR,\,H\alpha}}\ /\ \mathrm{M_\odot\ yr^{-1}\ kpc^{-2}}) > -1.6$.

2010; Rowlands et al. 2014; Rémy-Ruyer et al. 2015). Furthermore, SFR has been found to increase both as the dust attenuation affecting the stellar populations increases (e.g Tress et al. 2018), and as the dust attenuation derived from measurements of the Balmer decrement increases (e.g Garn & Best 2010; Zahid et al. 2012, 2017). However, the studies undertaken by these authors analysed only the global properties of galaxies; the advantage of this work is to demonstrate that local $\Sigma_{\mathrm{SFR,\,H\alpha}}$ variations have more influence than purely global quantities on dust attenuation properties.

The local $A_{V,\,\mathrm{gas}}$ excess also increases for increasing $\Sigma_{\mathrm{SFR,\,H\alpha}}$, which implies that the dependence of the local $A_{V,\,\mathrm{gas}}$ is not dominated by the dust attenuation due to the diffuse ISM alone. Finally, the $A_{V,\,\mathrm{stars}}/A_{V,\,\mathrm{gas}}$ ratio also increases as the $\Sigma_{\mathrm{SFR,\,H\alpha}}$ of the spaxels increases, despite the fact that both the numerator and denominator of this ratio increase with increasing $\Sigma_{\mathrm{SFR,\,H\alpha}}$. The other plots of Fig. 7 demonstrate why this is the case: while the dependence on $\Sigma_{\mathrm{SFR,\,H\alpha}}$ is strong for $A_{V,\,\mathrm{gas}}$, this dependence is stronger still for $A_{V,\,\mathrm{stars}}$. The $A_{V,\,\mathrm{stars}}/A_{V,\,\mathrm{gas}}$ ratio therefore increases for increasing $\Sigma_{\mathrm{SFR,\,H\alpha}}$. This result is in contrast to that found when considering the purely global properties of the galaxies in Fig. 3.

The results obtained from Fig. 7 provide a cautionary tale against putting too much stock in the mean global light- and volume-weighted quantities in Table 1 and the mean local volume-weighted quantities in Table 2. The mean local $A_{V,\,\mathrm{stars}}/A_{V,\,\mathrm{gas}}$ ratios in Table 2 especially are at odds with the distributions seen in Fig. 7, the peaks of which are distinct. For this reason, it is much more illuminating to interpret the results from the distributions of Fig. 3 and Fig. 7, rather than simply the mean values in Table 1 and Table 2.

The disparity between Fig. 3 and Fig. 7 implies that variations in dust attenuation properties are most likely driven more by local physics than by global physics. Locally, $A_{V,\,\mathrm{gas}}$ is strongly dependent on $\Sigma_{\mathrm{SFR,\,H\alpha}}$ because by isolating only those spaxels within galaxies with higher $\Sigma_{\mathrm{SFR,\,H\alpha}}$, a greater number of clumpy BCs associated with ongoing star formation should be expected. By contrast, when considering the galaxies globally this effect is washed out because each galaxy is likely to have regions of high $\mathrm{sSFR_{H\alpha}}$ balanced out by regions where the local $\mathrm{sSFR_{H\alpha}}$ is lower.

The difference between the global and local distributions for the dust attenuation affecting the stellar populations is not as pronounced. The peaks of the two separate sets of distributions are much closer together than those for the $A_{V,\,\mathrm{gas}}$ are. The distributions for $A_{V,\,\mathrm{stars}}$ in Fig. 3 and Fig. 7 will average over the clumpy dust since some stars will be in front of the diffuse, dusty ISM (experiencing little attenuation) and some will be behind. This means that there is not as much difference between the global and local $A_{V,\,\mathrm{stars}}$ distributions. In short, the results of Fig. 7 imply that while variations in the $A_{V,\,\mathrm{stars}}$ are probably a result of both local and global physics, variations in the $A_{V,\,\mathrm{gas}}$, by contrast, are predominantly driven by local physics.

5 THE GEOMETRY OF DUST IN STAR-FORMING SPIRAL GALAXIES

Let us now turn to an interpretation of these results. Models for the geometry of dust in SF galaxies – such as that depicted in Fig. 13 of Wild et al. (2011) – generally incorporate four key components:

(i) *Diffuse, dusty ISM:* Exhibits a radial gradient – the density of the ISM decreases with galactocentric radius.

(ii) *Young stars:* These highly ionising O and B stars are surrounded by H II regions, and thus produce nebular emission lines. These stars are located in the disk, and are still closely associated with their dusty, clumpy BCs.

(iii) *Intermediate age stars:* Also found in the disk. Less associated with BCs; attenuation from the ISM dominates.

(iv) *Old stars:* Found in the disk and bulge. Those behind the ISM will experience attenuation; those in front will not be attenuated by the ISM.

We are now equipped to test the validity of this model. When looking at separate galaxies on a spaxel-by-spaxel basis, as in Fig. 4 and Fig. 5, decreasing radial gradients are found for $A_{V,\,\mathrm{stars}}$. Such gradients can reasonably be attributed to the radial density gradient exhibited by the diffuse, dusty ISM of the host galaxies (e.g. Peletier et al. 1995; Boissier et al. 2004; Muñoz-Mateos et al. 2009; Wild et al. 2011; González Delgado et al. 2015; Goddard et al. 2016).

Ostensibly, a similar explanation might plausibly account for the similar radial gradient exhibited by $A_{V,\,\mathrm{gas}}$, since a 'screen-like' dust attenuation due to the ISM would affect both the old and the young stellar populations in a similar manner. However, this is not in fact the case; such gradients in the dust attenuation derived from the Balmer decrement

Downloaded from https://academic.oup.com/mnras/advance-article-abstract/doi/10.1093/mnras/staa1300/5838054 by guest on 18 May 2020

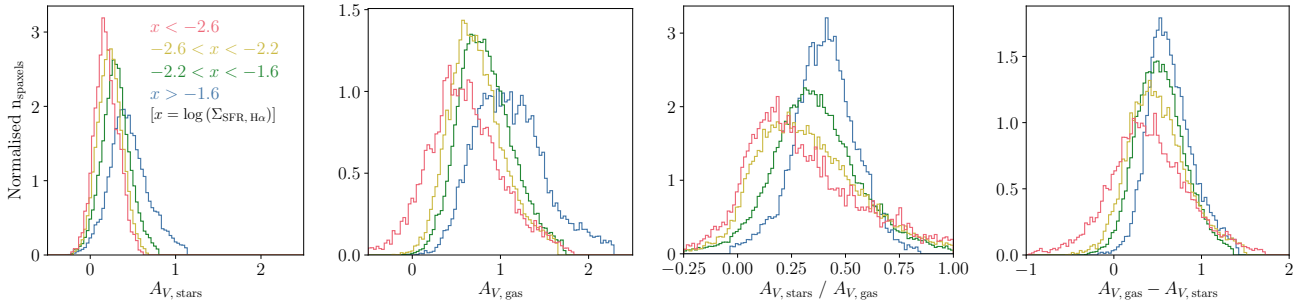

Figure 7. Distributions of (from left to right) A_V dust attenuation affecting the stellar populations, A_V dust attenuation derived from the Balmer decrement, the ratio of the two quantities, and the difference between the two quantities. The bins have been volume-weighted, and are normalised so that the area under each line is equal to one. The red histograms comprise spaxels with the lowest $\Sigma_{\rm SFR,\,H\alpha}$, in the range $\log(\Sigma_{\rm SFR,\,H\alpha}$ / M$_\odot$ yr^{-1} kpc$^{-2}) < -2.6$; yellow have $-2.6 < \log(\Sigma_{\rm SFR,\,H\alpha}$ / M$_\odot$ yr^{-1} kpc$^{-2}) < -2.2$; green have $-2.2 < \log(\Sigma_{\rm SFR,\,H\alpha}$ / M$_\odot$ yr^{-1} kpc$^{-2}) < -1.6$; and blue have the highest $\Sigma_{\rm SFR,\,H\alpha}$, in the range $\log(\Sigma_{\rm SFR,\,H\alpha}$ / M$_\odot$ yr^{-1} kpc$^{-2}) > -1.6$.

Table 2. Mean volume-weighted local A_V dust attenuation affecting the stellar populations, A_V dust attenuation derived from the Balmer decrement, the ratio of the two quantities, and the difference of the two quantities for each of the re-defined galaxy categories. The standard errors on the mean are quoted to 1σ.

$\log(\Sigma_{\rm SFR,\,H\alpha})$ [M$_\odot$ yr^{-1} kpc^{-2}]	Mean $A_{V,\,\rm stars}$	Mean $A_{V,\,\rm gas}$	Mean $A_{V,\,\rm stars}/A_{V,\,\rm gas}$	Mean $A_{V,\,\rm gas} - A_{V,\,\rm stars}$
$\log(\Sigma_{\rm SFR,\,H\alpha}) < -2.6$	0.191 ± 0.001	0.592 ± 0.004	0.335 ± 0.005	0.400 ± 0.004
$-2.6 < \log(\Sigma_{\rm SFR,\,H\alpha}) < -2.2$	0.2312 ± 0.0007	0.733 ± 0.002	0.338 ± 0.001	0.502 ± 0.002
$-2.2 < \log(\Sigma_{\rm SFR,\,H\alpha}) < -1.6$	0.3000 ± 0.0007	0.833 ± 0.001	0.3635 ± 0.0008	0.534 ± 0.001
$\log(\Sigma_{\rm SFR,\,H\alpha}) > -1.6$	0.454 ± 0.002	1.108 ± 0.003	0.405 ± 0.001	0.643 ± 0.002

cannot be explained by a density gradient in the diffuse ISM alone. Both Fig. 3 and Table 1 show that the distributions of both the global light-weighted $A_{V,\,\rm stars}$ and $A_{V,\,\rm gas}$ increase as the relative global sSFR$_{\rm H\alpha}$ of the galaxy increases; this behaviour is a natural consequence of a diffuse ISM which is denser for galaxies with higher sSFRs (e.g. Da Cunha et al. 2008, 2010; Rowlands et al. 2014; Rémy-Ruyer et al. 2015). However, the ratio of the two attenuation measures is not dependent upon the relative global sSFR$_{\rm H\alpha}$ of the galaxy. This result is in stark contrast to Fig. 7, in which each of the local $A_{V,\,\rm stars}$, the local $A_{V,\,\rm gas}$, and the local $A_{V,\,\rm stars}/A_{V,\,\rm gas}$ all increase as the local $\Sigma_{\rm SFR,\,H\alpha}$ increases. This behaviour suggests that while the radial gradient in $A_{V,\,\rm stars}$ is likely due to a combination of local and global physics (i.e. a diffuse ISM with a radial profile), the seemingly similar gradient in $A_{V,\,\rm gas}$ is instead dominated by purely local physics.

The above results suggest that the concentration of BCs (and associated young stars) increases towards the centre of SF spiral galaxies. Radial gradients have been found in SF galaxies for the dust attenuation derived from the Balmer decrement, which we reiterate is a proxy for the dust attenuation due to the BCs (e.g. Nelson et al. 2015a; Jafariyazani et al. 2019); SFR per unit physical surface area (e.g. Nelson et al. 2015b; González Delgado et al. 2016; Medling et al. 2018; Sánchez 2019); and the gas mass per unit physical surface area (e.g. Bigiel et al. 2008; Colombo et al. 2017; Sánchez 2019; see also Bolatto et al. 2017 and Lin et al. 2017 who find that the molecular gas content of galaxies peaks at their centres). The fact that all of these closely linked quantities are found to monotonically decrease with distance from the centres of SF galaxies suggests that the same may well be true for the concentration of BCs. The increase in molecular gas at the centres of spiral galaxies, seen both by radio (e.g Bigiel et al. 2008) and IFU (e.g. Lin et al. 2017; Colombo et al. 2017; Sánchez 2019) observations, is especially indicative of centrally concentrated BCs. This is because the molecular gas surface density is related to $\Sigma_{\rm SFR}$ by the Schmidt–Kennicutt Law (Schmidt 1959; Kennicutt 1998). We refer the reader to Bigiel et al. (2008) to see how well $\Sigma_{\rm SFR}$ is linked to the molecular gas content of galaxies.

A schematic diagram depicting the dust geometry of SF spiral galaxies described above is shown in Fig. 8. This dust geometry is similar to that suggested by Fig. 13 of Wild et al. (2011), except that in Fig. 8 we explicitly depict the radial dependence of the BCs, since we find direct evidence for such behaviour. The radial gradients seen for $A_{V,\,\rm stars}$ and the $A_{V,\,\rm gas}$ excess in Fig. 4 and Fig. 5 can be explained by the geometry in Fig. 8. The line of sight of Observer 1 is far from the galactic centre; therefore, Observer 1 will find low $A_{V,\,\rm stars}$ due to the radial dependence of the ISM, and almost zero $A_{V,\,\rm gas}$ excess due to the absence of BCs along their line of sight. By contrast, Observer 2 has a line of sight close to the galactic centre, and will consequently find higher values for both $A_{V,\,\rm stars}$ and the $A_{V,\,\rm gas}$ excess.

Further evidence for the concentration of clumpy BCs increasing nearer to the centre of SF spiral galaxies can be found in Fig. 4, in which the $A_{V,\,\rm gas}$ excess exhibits a radial gradient in all but the lowest-mass galaxies. This behaviour suggests that the radial gradient in the $A_{V,\,\rm gas}$ is produced by a combination of radial gradients in both the diffuse dusty ISM and the clumpy BCs. The radial gradient in the $A_{V,\,\rm gas}$ excess becomes progressively more pronounced for higher-mass galaxies; more massive galaxies, therefore, have clumpier dust distributions and a greater amount of clumpy dust nearer to their centres than less massive galaxies. Fig. 3 shows that stellar mass is indeed much more important than relative sSFR for determining the global dust and gas properties of a galaxy; this result is in agreement with the find-

Downloaded from https://academic.oup.com/mnras/advance-article-abstract/doi/10.1093/mnras/staa1300/5838054 by guest on 18 May 2020

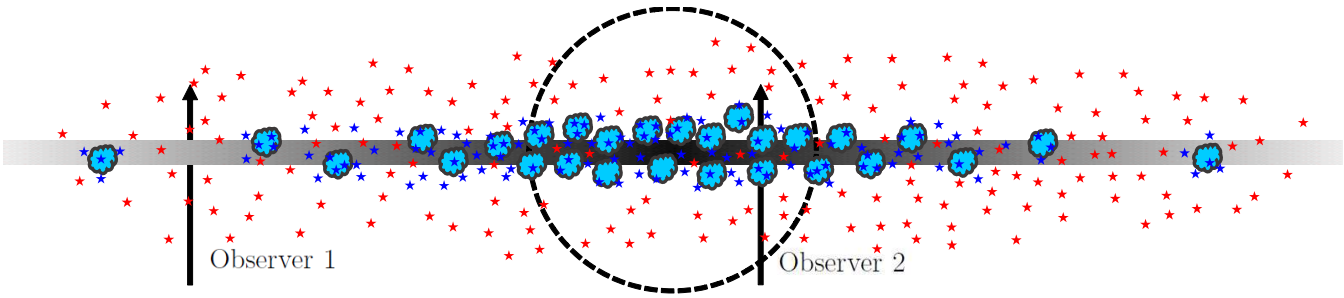

Figure 8. Schematic diagram showing an edge-on view of a SF spiral galaxy. Depicted are four key components: *a diffuse, dusty ISM* with a radial gradient (grey); *dusty, clumpy BCs* surrounded by H II regions (light blue clouds); *young stars* either embedded in, or still closely associated with, these BCs (dark blue stars); and *intermediate / old stars* further from their BCs (red stars). No assumptions are made about the bulge of the galaxy (dashed black line). Shown also are the lines of sight of two observers. Observer 1 will see a small amount of dust attenuation affecting the stellar populations, but no dust attenuation due to the clumpy BCs; Observer 2, however, will see high dust attenuation both due to the diffuse ISM and the clumpy BCs. The results in this work suggest that in addition to the presence of a diffuse, dusty ISM, SF spiral galaxies also exhibit a higher concentration of young stars and dusty BCs nearer to their central regions than at their outskirts.

ings of others such as Garn & Best (2010) and Zahid et al. (2012). It is stellar mass that is the dominant factor in determining these global properties, since higher stellar masses cause both higher SFRs (e.g Brinchmann et al. 2004; Noeske et al. 2007; Peng et al. 2010; Whitaker et al. 2012) and higher gas metallicities (e.g. Tremonti et al. 2004; Mannucci et al. 2010; Garn & Best 2010; Zahid et al. 2012). Galaxies with higher stellar masses have higher gas metallicities because they are able to retain a greater proportion of their metals (e.g. Tremonti et al. 2004); this in turn leads to increased dust attenuation, since a greater amount of metals are locked into dust grains (Heckman et al. 1998; Boissier et al. 2004).

In summary, not only do higher-mass galaxies have higher dust attenuations in the diffuse ISM, but they also have even higher dust attenuations due to their BCs. The dust geometry in high-mass galaxies must therefore be clumpier than in low-mass galaxies. Furthermore, a greater concentration of BCs is found nearer to the centres of high-mass galaxies than at their outskirts. This in turn suggests that star formation may be more centrally concentrated in higher-mass SF spiral galaxies.

6 CONCLUSIONS

We quantify the dust attenuation for 232 star-forming (SF) MaNGA spirals using two complementary methods. The Balmer decrement is determined across each galaxy's spaxels, and used to measure the dust attenuation in the gas. This quantity is compared with the dust attenuation affecting the stellar populations of each galaxy, ascertained using the full-spectrum stellar population synthesis code `STARLIGHT` (Cid Fernandes et al. 2005). The results in this work can be summarised as follows:

(i) The mean global light-weighted dust attenuation affecting the stellar populations ($A_{V,\,\mathrm{stars}}$) is consistently lower than the mean global light-weighted dust attenuation derived from the Balmer decrement ($A_{V,\,\mathrm{gas}}$). The mean $A_{V,\,\mathrm{stars}}$ is not strongly affected by the stellar mass of the galaxy, but the mean $A_{V,\,\mathrm{gas}}$ increases for increasing stellar mass. Both the mean values of $A_{V,\,\mathrm{stars}}$ and $A_{V,\,\mathrm{gas}}$ decrease as the global Hα derived specific star formation rate (sSFR$_{\mathrm{H}\alpha}$) relative to the star-forming main sequence (SFMS) of the galaxy decreases. The ratio of these two attenuation measures decreases for increasing stellar mass, but is independent of the global sSFR$_{\mathrm{H}\alpha}$ relative to the SFMS of the galaxy. The calculated ratios are comparable to, but consistently lower than, those found by Calzetti et al. (2000).

(ii) No difference is found for any of the local dust attenuation quantities analysed in this work between the spiral arm and inter-arm regions of the galaxies. This null result can largely be attributed to the relatively poor spatial resolution of MaNGA, which is unable to resolve narrow dust lanes within the spiral arms. As such, this investigation would be worth revisiting with higher resolution data.

(iii) Both the local $A_{V,\,\mathrm{stars}}$ and $A_{V,\,\mathrm{gas}}$ decrease with galactocentric radius, in agreement with the findings of González Delgado et al. (2015); Goddard et al. (2016) ($A_{V,\,\mathrm{stars}}$) and Nelson et al. (2015a); Jafariyazani et al. (2019) ($A_{V,\,\mathrm{gas}}$). By contrast, the local $A_{V,\,\mathrm{stars}}/A_{V,\,\mathrm{gas}}$ ratio does not vary between the centre of SF spiral galaxies and their outer regions (out to 1.5 R_{e}). The exception is the lowest-mass galaxies, which exhibit some radial gradient for this ratio due to the absence of such a gradient in their local $A_{V,\,\mathrm{gas}}$.

(iv) We introduce a new dust attenuation quantity, which we coin the $A_{V,\,\mathrm{gas}}$ excess (defined as $A_{V,\,\mathrm{gas}}-A_{V,\,\mathrm{stars}}$). This quantity, unlike the $A_{V,\,\mathrm{stars}}/A_{V,\,\mathrm{gas}}$ ratio, is physically meaningful, providing an estimate for the dust attenuation due the birth clouds (BCs) alone. A radial gradient is also exhibited by the $A_{V,\,\mathrm{gas}}$ excess, thus demonstrating that the radial gradient in the local $A_{V,\,\mathrm{gas}}$ cannot be attributed to a gradient in the diffuse ISM alone; the concentration of clumpy dust must also increase nearer to the galactic centre.

(v) We utilise the spatial resolution of MaNGA to analyse the the local values of each of $A_{V,\,\mathrm{stars}}$, $A_{V,\,\mathrm{gas}}$, $A_{V,\,\mathrm{stars}}/A_{V,\,\mathrm{gas}}$, and $A_{V,\,\mathrm{gas}}$ excess. Each of these quantities increases as the local star formation rate per unit physical surface area increases. These results suggest that variations in dust attenuation properties are likely driven predominantly by local physics, rather than the global properties of the galaxies.

(vi) The results in this work are consistent with the model

Downloaded from https://academic.oup.com/mnras/advance-article-abstract/doi/10.1093/mnras/staa1300/5838054 by guest on 18 May 2020

that stars are born in giant molecular BCs in which gas and very clumpy dust are highly concentrated (Lonsdale Persson & Helou 1987; Charlot & Fall 2000; Calzetti et al. 2000). However, this work demonstrates that the dust geometry in high-mass galaxies is clumpier than in low-mass galaxies. Furthermore, SF spiral galaxies are also shown to exhibit a much higher concentration of both young stars and BCs nearer to their central regions than at their outskirts.

ACKNOWLEDGEMENTS

We thank the anonymous referee for their very positive and useful comments and suggestions included in their review.

Funding for the Sloan Digital Sky Survey IV has been provided by the Alfred P. Sloan Foundation, the U.S. Department of Energy Office of Science, and the Participating Institutions. SDSS acknowledges support and resources from the Center for High-Performance Computing at the University of Utah. The SDSS website is `www.sdss.org`.

SDSS is managed by the Astrophysical Research Consortium for the Participating Institutions of the SDSS Collaboration including the Brazilian Participation Group, the Carnegie Institution for Science, Carnegie Mellon University, the Chilean Participation Group, the French Participation Group, Harvard-Smithsonian Center for Astrophysics, Instituto de Astrofísica de Canarias, The Johns Hopkins University, Kavli Institute for the Physics and Mathematics of the Universe (IPMU) / University of Tokyo, the Korean Participation Group, Lawrence Berkeley National Laboratory, Leibniz Institut für Astrophysik Potsdam (AIP), Max-Planck-Institut für Astronomie (MPIA Heidelberg), Max-Planck-Institut für Astrophysik (MPA Garching), Max-Planck-Institut für Extraterrestrische Physik (MPE), National Astronomical Observatories of China, New Mexico State University, New York University, University of Notre Dame, Observatório Nacional / MCTI, The Ohio State University, Pennsylvania State University, Shanghai Astronomical Observatory, United Kingdom Participation Group, Universidad Nacional Autónoma de México, University of Arizona, University of Colorado Boulder, University of Oxford, University of Portsmouth, University of Utah, University of Virginia, University of Washington, University of Wisconsin, Vanderbilt University, and Yale University.

This publication uses data generated via the `zooniverse.org` platform, development of which is funded by generous support, including a Global Impact Award from Google, and by a grant from the Alfred P. Sloan Foundation. This publication has been made possible by the participation of almost 6000 volunteers in the Galaxy Zoo:3D project on `zooniverse.org`.

This research made use of `Astropy`, a community-developed core `Python` (`https://www.python.org`) package for Astronomy (Robitaille et al. 2013); `Matplotlib` (Hunter 2007); `NumPy` (Van der Walt et al. 2011); `SciPy` (Virtanen et al. 2019); and `TOPCAT` (Taylor 2005).

M.B. acknowledges the FONDECYT regular grant 1170618. This work was supported by the Science and Technology Facilities Council.

REFERENCES

Abazajian K. N., et al., 2009, ApJS, 182, 543
Asa'd R. S., Vazdekis A., Cervino M., Noel N. E. D., Beasley M. A., Kassab M., 2017, MNRAS, 471, 3599
Baldwin J. A., Phillips M. M., Terlevich R., 1981, PASP, 93, 5
Belfiore F., et al., 2015, MNRAS, 449, 867
Belfiore F., et al., 2016, MNRAS, 461, 3111
Belfiore F., et al., 2019, AJ, 158, 160
Bell E. F., Kennicutt Jr. R. C., 2001, ApJ, 548, 681
Bertelli G., Bressan A., Chiosi C., Fagotto F., Nasi E., 1994, A&AS, 106, 275
Bigiel F., Leroy A., Walter F., Brinks E., de Blok W. J. G., Madore B., Thornley M. D., 2008, AJ, 136, 2846
Blanton M. R., Roweis S., 2006, AJ, 133, 734
Blanton M. R., et al., 2005, AJ, 129, 2562
Blanton M. R., Kazin E., Muna D., Weaver B. A., Price-Whelan A., 2011, AJ, 142, 31
Blanton M. R., et al., 2017, AJ, 154, 28
Boggess A., et al., 1978, Nature, 275, 372
Boissier S., Boselli A., Buat V., Donas J., Milliard B., 2004, A&A, 424, 465
Bolatto A. D., et al., 2017, ApJ, 846, 159
Boselli A., Gavazzi G., 2006, PASJ, 118, 517
Brinchmann J., Charlot S., White S. D. M., Tremonti C., Kauffmann G., Heckman T., Brinkmann J., 2004, MNRAS, 351, 1151
Buat V., Deharveng J. M., Donas J., 1989, A&A, 223, 42
Buat V., et al., 2006, ApJS, 173, 404
Bundy K., et al., 2015, ApJ, 798, 7
Calzetti D., 2001, PASP, 113, 1449
Calzetti D., Kinney A. L., Storchi-Bergmann T., 1994, ApJ, 429, 582
Calzetti D., Armus L., Bohlin R. C., Kinney A. L., Koornneef J., Storchi-Bergmann T., 2000, ApJ, 533, 682
Catalán-Torrecilla C., et al., 2015, A&A, 584, A87
Chabrier G., 2003, PASP, 115, 763
Chandar R., et al., 2017, ApJ, 845, 78
Charlot S., Fall S. M., 2000, ApJ, 539, 718
Cherinka B., et al., 2018, AJ, 158, 74
Cid Fernandes R., 2018, MNRAS, 480, 4480
Cid Fernandes R., González Delgado R. M., 2009, MNRAS, 403, 780
Cid Fernandes R., Mateus A., Sodré L., Stasińska G., Gomes J. M., 2005, MNRAS, 358, 363
Colombo D., et al., 2017, MNRAS, 475, 1791
Da Cunha E., Charlot S., Elbaz D., 2008, MNRAS, 388, 1595
Da Cunha E., Eminian C., Charlot S., Blaizot J., 2010, MNRAS, 403, 1894
Dalcanton J. J., Yoachim P., Bernstein R. A., 2004, ApJ, 608, 189
Domínguez A., et al., 2013, ApJ, 763, 145
Driver S. P., Popescu C. C., Tuffs R. J., Liske J., Graham A. W., Allen P. D., De Propris R., 2007, MNRAS, 379, 1022
Drory N., et al., 2015, AJ, 149, 77
Egusa F., Sofue Y., Nakanishi H., 2004, PASJ, 56, L45
Fanelli M. N., O'Connell R. W., Thuan T. X., 1988, ApJ, 334, 665
Feltzing S., Bowers J. B., Agertz O., 2020, MNRAS, 493, 1419
Frankel N., Rix H.-W., Ting Y.-S., Ness M. K., Hogg D. W., 2018, ApJ, 865, 96
Fraser-McKelvie A., Merrifield M., Aragón-Salamanca A., 2019, MNRAS, 489, 5030
Garn T., Best P., 2010, MNRAS, 409, 421
Ge J., Yan R., Cappellari M., Mao S., Li H., Lu Y., 2018, MNRAS, 478, 2633
Gilbank D. G., Baldry I. K., Balogh M. L., Glazebrook K., Bower R. G., 2010, MNRAS, 405, 2594
Giovanelli R., Haynes M. P., Salzer J. J., Wegner G., da Costa

Downloaded from https://academic.oup.com/mnras/advance-article-abstract/doi/10.1093/mnras/staa1300/5838054 by guest on 18 May 2020

L. N., Freudling W., 1995, AJ, 110, 1059
Girardi L., Bressan A., Bertelli G., Chiosi C., 1999, A&AS, 141, 371
Glazebrook K., Blake C., Economou F., Lilly S., Colless M., 1999, MNRAS, 306, 843
Goddard D., et al., 2016, MNRAS, 466, 4731
González Delgado R. M., et al., 2015, A&A, 581, A103
González Delgado R. M., et al., 2016, A&A, 590, A44
Grootes M. W., et al., 2017, AJ, 153, 111
Groves B., Brinchmann J., Walcher C. J., 2012, MNRAS, 419, 1402
Gunn J. E., et al., 2006, AJ, 131, 2332
Guo K., Zheng X. Z., Wang T., Fu H., 2015, ApJ, 808, L49
Hart R. E., et al., 2016, MNRAS, 461, 3663
Heckman T. M., Robert C., Leitherer C., Garnett D. R., van der Rydt F., 1998, ApJ, 503, 646
Holwerda B. W., Gonzalez R. A., Allen R. J., van der Kruit P. C., 2004, AJ, 129, 1396
Holwerda B. W., Bianchi S., Baes M., de Jong R. S., Dalcanton J. J., Radburn-Smith D., Gordon K., Xilouris M., 2012, IAUSymp, 284, 128
Hou L. G., Han J. L., 2015, MNRAS, 454, 626
Hunter J. D., 2007, Comput. Sci. Eng., 9, 90
Jafariyazani M., Mobasher B., Hemmati S., Fetherolf T., Khostovan A. A., Chartab N., 2019, ApJ, 887, 204
Kauffmann G., et al., 2003, MNRAS, 346, 1055
Keel W. C., 1993, ASPC, 35, 498
Kennicutt R. C., 1998, ApJ, 498, 541
Kennicutt R. C., et al., 2007, ApJ, 671, 333
Kewley L. J., Dopita M. A., Sutherland R. S., Heisler C. A., Trevena J., 2001, ApJ, 556, 121
Kewley L. J., Nicholls D. C., Sutherland R. S., 2019, ARA&A, 57, 511
Kreckel K., et al., 2013, ApJ, 771, A62
Law D. R., et al., 2015, AJ, 150, 19
Law D. R., et al., 2016, AJ, 152, 83
Li H., Wuyts S., Lei H., Lin L., Lam M. I., Boquien M., Andrews B. H., Schneider D. P., 2019, ApJ, 872, 63
Lin L., et al., 2017, ApJ, 851, 18
Loebman S. R., Roskar R., Debattista V. P., Ivezic Z., Quinn T. R., Wadsley J., 2010, ApJ, 737, 8
Lonsdale Persson C. J., Helou G., 1987, ApJ, 314, 513
Madau P., Ferguson H. C., Dickinson M. E., Giavalisco M., Steidel C. C., Fruchter A., 1996, MNRAS, 283, 1388
Mannucci F., Cresci G., Maiolino R., Marconi A., Gnerucci A., 2010, MNRAS, 408, 2115
Medling A. M., et al., 2018, MNRAS, 475, 5194
Minchev I., Famaey B., 2009, ApJ, 722, 112
Minchev I., et al., 2018, MNRAS, 481, 1645
Muñoz-Mateos J. C., et al., 2009, ApJ, 701, 1965
Nelson E. J., et al., 2015a, ApJ, 817, L9
Nelson E. J., et al., 2015b, ApJ, 828, 27
Noeske K. G., et al., 2007, ApJ, 660, L43
O'Donnell J. E., 1994, ApJ, 422, 158
Osterbrock D. E., Ferland G. J., 2005, Astrophysics of Gaseous Nebulae and Active Galactic Nuclei, 2nd ed., University Science Books
Pannella M., et al., 2009, ApJ, 698, L116
Pannella M., et al., 2015, ApJ, 807, 141
Peletier R. F., Valentijn E. A., Moorwood A. F. M., Freudling W., Knapen J. H., Beckman J. E., 1995, A&A, 300, L1
Peng Y.-J., et al., 2010, ApJ, 721, 193
Peterken T., et al., 2019, MNRAS, 489, 1338
Price S. H., et al., 2014, ApJ, 788, 86
Rémy-Ruyer A., et al., 2015, A&A, 582, A121
Roberts W. W., 1969, ApJ, 158, 123
Robitaille T. P., et al., 2013, A&A, 558
Rodríguez del Pino B., et al., 2017, MNRAS, 467, 4200
Roškar R., Debattista V. P., Quinn T. R., Stinson G. S., Wadsley J., 2008, ApJ, 684, L79
Rowlands K., et al., 2014, MNRAS, 441, 1017
Salim S., Narayanan D., 2020, preprint (arXiv:2001.03181)
Salim S., Boquien M., Lee J. C., 2018, ApJ, 859, 11
Sánchez S. F., 2019, preprint (arXiv:1911.06925)
Sánchez S. F., et al., 2012, A&A, 538, A8
Schaefer A. L., et al., 2017, MNRAS, 464, 121
Schaefer A. L., et al., 2018, MNRAS, 483, 2851
Schmidt M., 1959, ApJ, 129, 243
Sellwood J. A., Binney J. J., 2002, MNRAS, 336, 785
Shabani F., et al., 2018, MNRAS, 478, 3590
Simard L., Mendel J. T., Patton D. R., Ellison S. L., McConnachie A. W., 2011, ApJS, 196, 11
Smee S. A., et al., 2013, AJ, 146, 32
Spindler A., et al., 2017, MNRAS, 476, 580
Steidel C. C., Adelberger K. L., Giavalisco M., Dickinson M., Pettini M., 1999, ApJ, 519, 1
Storchi-Bergmann T., Calzetti D., Kinney A. L., 1994, ApJ, 429, 572
Sullivan M., Treyer M. A., Ellis R. S., Bridges T. J., Milliard B., Donas J., 2000, MNRAS, 312, 442
Tamburro D., Rix H. W., Walter F., Brinks E., de Blok W. J. G., Kennicutt R. C., Mac Low M. M., 2008, AJ, 136, 2872
Taylor M. B., 2005, Astronomical Data Analysis Software and Systems XIV - ASP Conference Series, 347, 29
Tremonti C. A., et al., 2004, ApJ, 613, 898
Tress M., et al., 2018, MNRAS, 475, 2363
Urrutia T., et al., 2019, A&A, 624, A141
Van der Walt S., Colbert S. C., Varoquaux G., 2011, Comput. Sci. Eng., 13, 22
Vazdekis A., Sánchez-Blázquez P., Falcón-Barroso J., Cenarro A. J., Beasley M. A., Cardiel N., Gorgas J., Peletier R. F., 2010, MNRAS, 404, 1639
Vazdekis A., Koleva M., Ricciardelli E., Röck B., Falcón-Barroso J., 2016, MNRAS, 463, 3409
Veilleux S., Osterbrock D. E., 1987, ApJS, 63, 295
Virtanen P., et al., 2019, preprint (arXiv:1907.10121)
Wake D. A., et al., 2017, AJ, 154, 86
Walborn N. R., Barbá R. H., Brandner W., Rubio M., Grebel E. K., Probst R. G., 1999, AJ, 117, 225
Westfall K. B., et al., 2019, AJ, 158, 231
Whitaker K. E., van Dokkum P. G., Brammer G., Franx M., 2012, ApJ, 754, L29
White R. E., Keel W. C., 1992, Nature, 359, 129
White R. E., Keel W. C., Conselice C. J., 2000, ApJ, 542, 761
Wild V., Charlot S., Brinchmann J., Heckman T., Vince O., Pacifici C., Chevallard J., 2011, MNRAS, 417, 1760
Wilkinson D. M., et al., 2015, MNRAS, 449, 328
Willett K. W., et al., 2013, MNRAS, 435, 2835
Wuyts S., et al., 2013, ApJ, 779, 135
Xilouris E. M., Byun Y. I., Kylafis N. D., Paleologou E. V., Papamastorakis J., 1999, A&A, 344, 868
Yan R., et al., 2016a, AJ, 151, 8
Yan R., et al., 2016b, AJ, 152, 197
Yi S. K., 2008, ASP Conference Series, 392, 3
Zahid H. J., Yates R. M., Kewley L. J., Kudritzki R.-P., 2012, ApJ, 763, 92
Zahid H. J., et al., 2017, ApJ, 847, 18

This paper has been typeset from a TEX/LATEX file prepared by the author.

Downloaded from https://academic.oup.com/mnras/advance-article-abstract/doi/10.1093/mnras/staa1300/5838054 by guest on 18 May 2020